

Identification strategies for model-based control

Laurent Cordier · Bernd R. Noack · Gilles Tissot ·
Guillaume Lehnasch · Joël Delville · Maciej Balajewicz ·
Guillaume Daviller · Robert K. Niven

Received: 16 May 2012/Revised: 2 June 2013/Accepted: 6 July 2013
© Springer-Verlag Berlin Heidelberg 2013

Abstract A reduced-order modelling (ROM) strategy is crucial to achieve model-based control in a wide class of flow configurations. In turbulence, ROMs are mostly derived by Galerkin projection of first-principles equations onto the proper orthogonal decomposition (POD) modes. These POD ROMs are known to be relatively fragile when used for control design. To understand more deeply this behaviour, a hierarchy of POD ROMs is studied and compared for a two-dimensional uncontrolled mixing layer. First, dynamical models based on POD are derived from the Navier–Stokes and the vorticity equations. It is shown that these models can exhibit for some truncation level finite-time blow-ups. A symmetrized quadratic model is then proposed to enforce the preservation of energy in the model. This formulation improves considerably the behaviour of the model, but the energy level is still over-estimated. Subsequently, a nonlinear eddy-viscosity model

with guaranteed stability is proposed. This model still leads to an imperfect description of the energy. Different 4D-Var identification strategies are then considered to improve the nonlinear eddy-viscosity model. It is shown that penalizing the time variation in the eddy-viscosity parameter leads to the best compromise in terms of description of the energy and of physical relevance of the eddy viscosity. Lastly, a statistical inference procedure is used to take into account the bias inherent of the sampling employed in the identification procedure. Joined probability density functions are then determined empirically for all the coefficients of the model, and a stochastic dynamical model is finally derived to study the influence on the long-term solution of different equiprobable sets of coefficients.

1 Introduction

A hierarchy of POD Galerkin models is studied and compared for a two-dimensional (2D) mixing layer configuration. These reduced-order models are a part of plant hierarchy for model-based control. Control design may be performed in a model-free manner or based on black-box, grey-box and white-box models—following a classification of Wiener (1948). Model-free control, like extremum/slope seeking (Krstic et al. 1999), optimizes parameters of working open-loop forcing in a self-adaptive manner on long time scales. In-time disturbance rejection requires at minimum a black-box model characterizing the input-output response. Such a predominantly linear model may be obtained from experimental forcing studies. Grey-box models resolve in addition to the input-output behaviour also the resulting coherent structure manipulation in a low-order manner. Examples are vortex (see, e.g. Lugt 1996; Wu et al. 2006) and Galerkin models (see, e.g. Fletcher

This article is part of the collection Topics in Flow Control. Guest Editors J. P. Bonnet and L. Cattafesta.

L. Cordier (✉) · B. R. Noack · G. Tissot · G. Lehnasch ·
J. Delville · G. Daviller
Institut Pprime, CNRS – Université de Poitiers – ENSMA,
UPR 3346, Département Fluides, Thermique, Combustion,
CEAT, 43 rue de l’Aérodrome, 86036 Poitiers Cedex, France
e-mail: Laurent.Cordier@univ-poitiers.fr

M. Balajewicz
Mechanical Engineering and Materials Sciences,
Duke University, Durham, NC 27708-0287, USA
e-mail: Maciej.Balajewicz@duke.edu

R. K. Niven
School of Engineering and Information Technology,
The University of New South Wales at ADFA,
Canberra, ACT 2600, Australia
e-mail: R.Niven@adfa.edu.au

1984). Galerkin models are well suited for control design (see, e.g. Noack et al. 2011). In contrast, the hybrid nature of vortex models with generation, annihilation and merging of vortices challenges most control design methods.

This study concerns low-order Galerkin models. In a simple case of a stationary domain Ω and stationary boundary conditions at $\partial\Omega$, the velocity field \mathbf{u} may be approximated by a Galerkin expansion with a basic mode \mathbf{u}_0, N space-dependent expansion modes $\mathbf{u}_i, i = 1, \dots, N$ with corresponding time-dependent amplitudes a_i :

$$\mathbf{u}(\mathbf{x}, t) = \mathbf{u}_0(\mathbf{x}) + \sum_{i=1}^N a_i(t)\mathbf{u}_i(\mathbf{x}) = \sum_{i=0}^N a_i(t)\mathbf{u}_i(\mathbf{x}), \quad \text{with} \\ a_0 \triangleq 1. \quad (1)$$

The modes may result from a priori completeness considerations (see, e.g. Ladyzhenskaya 1963; Noack and Eckelmann 1994), from Navier–Stokes-based eigenproblems (see, e.g. Joseph 1976), or a posteriori from flow data, like the proper orthogonal decomposition (POD) (see, e.g. Holmes et al. 2012) or the dynamic mode decomposition (DMD) (Rowley et al. 2009; Schmid 2010). Here, POD modes are employed.

The evolution equation for the state $\mathbf{a} = (a_1, \dots, a_N)$ is an autonomous system of ordinary differential equations

$$\frac{d}{dt}\mathbf{a} = \mathbf{f}(\mathbf{a}, \mathbf{y}) + \mathbf{f}_c(\mathbf{a}, \mathbf{z}, \mathbf{c}), \quad (2)$$

where (see Cordier et al. 2010) \mathbf{y} and \mathbf{z} denote the model coefficients corresponding, respectively, to the uncontrolled and controlled part of the dynamics, and where \mathbf{c} are the control parameters. The propagators \mathbf{f} and \mathbf{f}_c may be derived a priori from the Navier–Stokes equations via a Galerkin projection onto the POD modes (Noack et al. 2011) or identified a posteriori from a reference solution (Perret et al. 2006; Cordier et al. 2010). Often, a combination of first-principle structure identification and empirical parameter identification is employed. In this paper, we investigate a full spectrum of identification strategies going from a priori to a posteriori methods, and we ignore actuation for reasons of simplicity.

As configuration, the mixing layer with velocity ratio 3:1 is chosen (Comte et al. 1998). On the one hand, this flow exhibits pronounced coherent structures, thus making it accessible to reduced-order modelling. On the other hand, dynamics is moderately complex due to a range of different frequencies to be resolved.

The paper is organized as follows: the employed mixing layer database is described in Sect. 2. In Sect. 3, Galerkin models are derived from first principles, the Navier–Stokes and the vorticity equations. In Sect. 4, the effects of unresolved velocity fluctuations are studied, including finite-time blow-ups. A nonlinear subgrid turbulence model

is proposed which yields guaranteed bounded solutions. Section 5 employs a 4D-Var method for the identification of few parameters in subgrid turbulence models to complete identification of the constant-linear-quadratic propagator. Such model identification techniques are necessary for most empirical flow data. The uncertainty of Galerkin system parameters is investigated in Sects. 6, and 7 summarizes the main findings as good practices. Finally, all the dynamical models are investigated numerically in “Appendix”, where their respective performance is judged based on the time evolution of the POD coefficients and their power spectra.

2 Mixing layer database

The database used for the present work corresponds to the direct numerical simulation (hereafter DNS) of a compressible isothermal 2D mixing layer as shown in Fig. 1. The numerical algorithm is the same as that employed previously for studies on jet noise sources (Cavaliere et al. 2011). The full NavierStokes equations for 3D fluid motion are formulated in Cartesian coordinates and solved in conservative form. Spatial derivatives are computed with a fourth-order-accurate finite scheme (Gottlieb and Turkel 1976) for both the inviscid and viscous portion of the flux (Hayder and Turkel 1993). A second-order predictor-corrector scheme is used to advance the solution in time. In addition, block decomposition and MPI parallelization are implemented. The three-dimensional Navier–Stokes characteristic nonreflective boundary conditions, developed in Lodato et al. (2008), are applied at the boundaries of the computational domain to account for convective fluxes and pressure gradients across the boundary plane. In order to simulate anechoic boundary conditions, the mesh is stretched and a dissipative term is added to the equations, in the sponge zone, following Colonius et al. (1993). A detailed description of the numerical procedure is given in Daviller (2010).

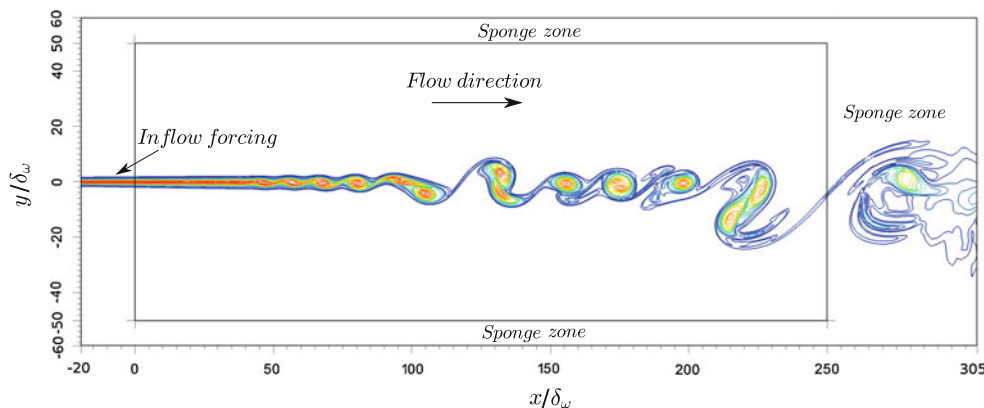
2.1 Flow configuration

The inflow mean streamwise velocity profile is given by a hyperbolic tangent profile

$$U(y) = U_2 + \frac{1}{2}\Delta U[1 + \tanh(2y)] \quad (3)$$

with $\Delta U = U_1 - U_2$ the velocity difference across the mixing layer, where U_1 and U_2 are the initial velocity above and below, respectively. The velocities, lengths and time are nondimensionalized with ΔU and the initial vorticity thickness δ_ω . The flow Reynolds number is $Re = \delta_\omega \Delta U / \nu_a = 500$ where the subscript $(\cdot)_a$ indicates a

Fig. 1 Visualization of a 2D mixing layer vorticity snapshot



constant ambient quantity. The Mach number of the free streams are $M_1 = U_1/c_a = 0.1$ and $M_2 = U_2/c_a = 0.033$, where c_a is the sound speed. The inflow mean temperature is calculated with the Crocco–Busemann relation, and the inflow mean pressure is constant. The Prandtl number is selected to be $Pr = 0.7$. Finally, the convective Mach number is given by $M_c = \Delta U/2c_a = 0.033$. Since $M_c < 0.3$, the flow can be assumed as quasi-incompressible (Gatski and Bonnet 2013). Figure 1 shows instantaneous isovalues of spanwise vorticity. The numerical code was extensively validated against numerical and experimental data; some results can be found in Daviller (2010) or Cavalieri et al. (2011).

2.2 Numerical specifications

The computations were performed on the cluster of the PPRIME Institute using 64 processors. The computational domain comprises approximately 2.1 million grid points: 2367 points in the streamwise direction, 884 points along the y direction and 3 points in the spanwise direction, leading to quasi 2D results. The 2D extension of the computational domain is $325\delta_\omega \times 120\delta_\omega$. The sponge regions are from $x = -20\delta_\omega$ to $x = 0$ and $x = 250\delta_\omega$ to $x = 305\delta_\omega$ in the streamwise direction, and from $\pm 50\delta_\omega$ to $\pm 60\delta_\omega$ in the transverse y direction (see Fig. 1). In the shear layer ($-10 \leq y/\delta_\omega \leq 10$), the grid spacing in the y direction is uniform and equal to $\Delta y_{\min} = 0.07\delta_\omega$. This value corresponds to the minimum grid spacing in the y direction. The grid is then stretched using error functions as in Wei (2004). The parameters of the stretching are chosen to give a maximum spacing $\Delta y_{\max} = 0.9\delta_\omega$ at $y = \pm 60\delta_\omega$. In the physical domain ($0 \leq x/\delta_\omega \leq 250$), the grid spacing in the x direction is uniform and equal to $\Delta x_{\min} = 1.7\Delta y_{\min}$. In the sponge regions, similar mapping functions are used along x , to match $\Delta x_{\max} = 0.9\delta_\omega$ at $x = -20\delta_\omega$ and $\Delta x_{\max} = 2\delta_\omega$ at $x = 305\delta_\omega$. To govern the development of the mixing layer, the flow is forced by adding at every iteration solenoidal perturbations defined as (see Bogey 2000):

$$\begin{aligned}
 u(x, y, t) &= u(x, y, t) + \alpha \epsilon(t) U_c \frac{(y - y_0)}{\Delta y_{\min}} \\
 &\quad \times \exp \left\{ -\ln(2) \frac{(x - x_0)^2 + (y - y_0)^2}{\Delta y_{\min}^2} \right\} \\
 v(x, y, t) &= v(x, y, t) - \alpha \epsilon(t) U_c \frac{(x - x_0)}{\Delta y_{\min}} \\
 &\quad \times \exp \left\{ -\ln(2) \frac{(x - x_0)^2 + (y - y_0)^2}{\Delta y_{\min}^2} \right\} \quad (4)
 \end{aligned}$$

where $-1 \leq \epsilon \leq 1$ is a random number, and $U_c = (U_1 + U_2)/2$ is the convection velocity. The simulation parameters are $x_0 = -5\delta_\omega$ and $y_0 = 0$ for the location of the excitation and $\alpha = 0.01$ for the forcing coefficient.

The simulation is first initialized over 330 000 time steps ($\Delta t = 1.8 \times 10^{-8}$ s) which correspond to a total run time of 35 h. The database is then generated: 1 093 695 iterations are done on 115 h to create $N_t = 2,000$ snapshots, sampled at $f_s = 100$ kHz.

3 Galerkin model from first principles

In the following, we assume an incompressible, viscous flow in steady domain Ω with time-independent boundary conditions at $\partial\Omega$, e.g. Dirichlet, Neumann, convective outflow or periodic conditions. All quantities are assumed to be normalized, and $\nu = 1/Re$ represents the inverse Reynolds number. The Galerkin model is based on the inner product between two square integrable velocity fields $\mathbf{u}, \mathbf{v} \in \mathcal{L}^2(\Omega)$:

$$(\mathbf{u}, \mathbf{v})_\Omega \triangleq \int_\Omega \mathbf{u} \cdot \mathbf{v} dx. \quad (5)$$

Two types of POD models derived from first principles are reviewed. The first kind (Sect. 3.1) employs the Navier–Stokes equations for the Galerkin projection. The advantage is that only first spatial derivatives of the POD

modes are required. The price is an auxiliary model for the pressure term. In Sect. 3.2, this explicit pressure term model is bypassed by employing the vorticity transport equation for Galerkin projection at the expense of second spatial derivatives of the modes.

3.1 Galerkin projection onto the Navier–Stokes equations

A standard Galerkin projection of the Navier–Stokes equations onto the POD modes expressed in (1) yields a Galerkin system (2) of the form (see, e.g. Noack et al. 2011)

$$\dot{a}_i = \nu \sum_{j=0}^N l_{ij}^v a_j + \sum_{j,k=0}^N q_{ijk}^c a_j a_k + \sum_{j,k=0}^N q_{ijk}^p a_j a_k. \tag{6}$$

The left-hand side arises from the local acceleration. The three terms on the right-hand side originate from the viscous, convective and pressure term, respectively. The dynamical system (6) is traditionally referred as POD Reduced-Order Model or POD ROM.

For confined flow, the pressure term vanishes identically $q_{ijk}^p \equiv 0$ (see, e.g. Holmes et al. 2012). For open flows, the pressure term is generally well represented by a constant linear fit with the mode amplitudes (Galletti et al. 2004; Noack et al. 2005):

$$(\mathbf{u}_i, -\nabla p(t))_\Omega = \sum_{j=0}^N l_{ij}^p a_j(t). \tag{7}$$

Here, $l_{ij}^p, i = 1, \dots, N, j = 0, \dots, N$ are obtained from a least-squares fit of (7) from DNS data for M snapshots ($M > N$). In the following, this empirical constant linear term is taken as pressure term representation in the Galerkin system:

$$\dot{a}_i = \nu \sum_{j=0}^N l_{ij}^v a_j + \sum_{j,k=0}^N q_{ijk}^c a_j a_k + \sum_{j=0}^N l_{ij}^p a_j. \tag{8}$$

The resulting model will be abbreviated as GS^u in the following. Its behaviour will be discussed in Sect. 4. For that, the turbulent kinetic energy (TKE) will be used for assessing the dynamical behaviour of the Galerkin system by comparison with the DNS database. A similar criterion was recently used in Balajewicz et al. (2013) for judging POD ROMs based on a new proposed stabilization methodology.

3.2 Galerkin projection onto the vorticity equation

The vorticity transport equation is obtained from the Navier–Stokes equations by taking the curl:

$$\frac{\partial \boldsymbol{\omega}}{\partial t} = \boldsymbol{\omega} \cdot \nabla \mathbf{u} - \mathbf{u} \cdot \nabla \boldsymbol{\omega} + \nu \Delta \boldsymbol{\omega}, \tag{9}$$

where $\boldsymbol{\omega} = \nabla \times \mathbf{u}$ is the vorticity vector. This formulation removes any complications from the pressure term by eliminating it all together. The vorticity field $\boldsymbol{\omega}$ is approximated by taking the curl of the Galerkin expansion (1):

$$\boldsymbol{\omega}(\mathbf{x}, t) = \boldsymbol{\omega}_0(\mathbf{x}) + \sum_{i=1}^N a_i^\omega(t) \boldsymbol{\omega}_i(\mathbf{x}), \tag{10}$$

with $\boldsymbol{\omega}_i = \nabla \times \mathbf{u}_i$ for $i = 0, \dots, N$. The Galerkin projection of (9) onto $\boldsymbol{\omega}_i, i = 1, \dots, N$ yields a system of ordinary differential equations

$$\sum_{j=1}^N m_{ij}^\omega \dot{a}_j^\omega = \nu \sum_{j=0}^N l_{ij}^{\omega,v} a_j^\omega + \sum_{j,k=0}^N q_{ijk}^{\omega,c} a_j^\omega a_k^\omega, \quad i = 1, \dots, N \tag{11}$$

where

$$\begin{aligned} m_{ij}^\omega &= (\boldsymbol{\omega}_i, \boldsymbol{\omega}_j)_\Omega, \\ q_{ijk}^{\omega,c} &= (\boldsymbol{\omega}_i, \boldsymbol{\omega}_j \cdot \nabla \mathbf{u}_k - \mathbf{u}_j \cdot \nabla \boldsymbol{\omega}_k)_\Omega, \\ l_{ij}^{\omega,v} &= (\boldsymbol{\omega}_i, \Delta \boldsymbol{\omega}_j)_\Omega. \end{aligned}$$

Similarly to (6), (11) is an evolution equation for the temporal amplitudes a_i^ω associated with the i th vorticity basis function. In contrast to (6), (11) contains no contributions from the pressure, but a mass matrix m_{ij}^ω is now present. This mass matrix that comes from the nonorthogonality of $\boldsymbol{\omega}_i$ must be inverted for integrating in time (11). However, the inverse of the mass matrix can be computed once for all at the beginning of the time integration, and the extra computational cost is hence low. Moreover, since in (6), the Galerkin projection is carried out on the velocity fields, while in (11), the Galerkin projection is carried out on the vorticity fields, the temporal amplitudes derived from solutions of (6) and (11) will in general not be identical. In practice, however, the quality of reduced-order models derived from (6) and (11) is comparable (Rempfer and Fasel 1994). The Galerkin system (11) will be called GS^ω.

Figure 2 illustrates the TKE of the two-dimensional mixing layer. The TKE is obtained from the employed direct numerical solution and predicted by Galerkin system (11) through:

$$K(t) = \sum_{i=1}^N K_i(t), \quad \text{where } K_i(t) \triangleq \frac{1}{2} a_i^2(t). \tag{12}$$

Contrary to the Galerkin system of Sect. 3.1, all Galerkin systems (11) $N = 10, 20, 50$ and 100 remain bounded. The accuracy increases, as expected, with the number of modes N .

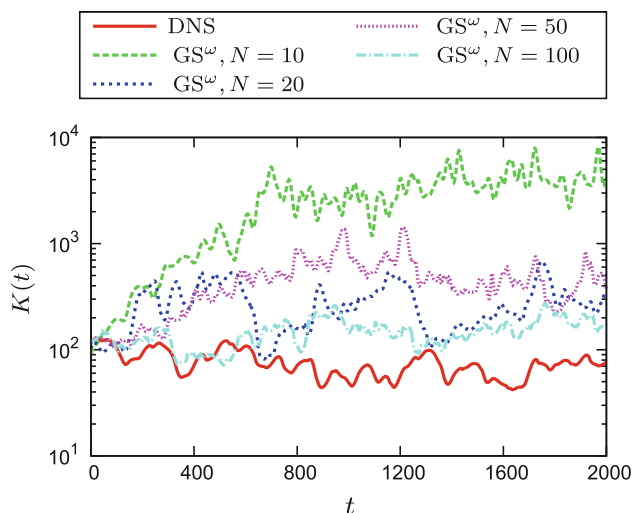


Fig. 2 Evolution of the TKE of the 2D mixing layer. Data of the DNS and of Galerkin systems (11) for different values of N are displayed (see caption)

4 Subgrid turbulence representation

In this section, we account for unresolved velocity fluctuations in the Galerkin model with a nonlinear eddy-viscosity term. First, in Sect. 4.1, a diverging solution of a Galerkin system without such subgrid turbulence representation is investigated. The quadratic term is found to have an important role in the observed unbounded growth. Then, in Sect. 4.2, the energy preservation of the quadratic term is enforced. This prevents unbounded growth, yet leads to too large fluctuation levels. Finally, in Sect. 4.3, a physically motivated simple nonlinear eddy-viscosity model is proposed. This model guarantees bounded Galerkin solutions for energy-preserving quadratic terms and yields a good resolution of the modal energy.

4.1 Analysis of a Galerkin system blow-up

Diverging POD model solutions are commonly observed (yet rarely published). The first reason is that autonomous quadratic differential equations as (6) and (11) are well known to exhibit sufficient condition of finite-time blow-up (Getz and Jacobson 1977). A second reason is that the stability properties of the Navier–Stokes solutions are not preserved under Galerkin projection. A stable Navier–Stokes solution may have an unstable Galerkin model solution even if the POD is fully accurate (Rempfer 2000; Noack et al. 2003). These types of instabilities may be cured by adding dynamically important zero-energy modes (Noack et al. 2003). A second reason is that the energy cascade from large to small structures may not be adequately resolved by the POD model. POD modes resolve the production much better than the dissipation. This leads

to an excess production of TKE in the POD subspace. Eddy-viscosity terms are the early and most natural cure (Aubry et al. 1988; Rempfer and Fasel 1994; Ukeiley et al. 2001). However, even these models with carefully calibrated eddy viscosities tend to be fragile (Sirisup and Karniadakis 2004).

In this subsection, the phenomenology and dynamics of unbounded POD model solutions are studied. First, the Galerkin system (8) with $N = 20$ —called GS^{TI} in the following—is analysed (see Table 1).

In all following Galerkin solutions, the initial condition $a_i(0), i = 1, \dots, N$ is taken from the first snapshot of the DNS, *i.e.*

$$a_i(0) = a_i^P(0) = (\mathbf{u}(\mathbf{x}, 0) - \mathbf{u}_0(\mathbf{x}), \mathbf{u}_i(\mathbf{x}))_\Omega, \tag{13}$$

where the superscript P denotes POD values coming directly from the DNS database. Galerkin solution I diverges shortly after $t = 2,000$ (see Fig. 3). By adding more modes, the behaviour of the Galerkin system is not cured and the divergence happens earlier.

In the following, the maximum growth rate of the Galerkin system TKE is estimated. All considered systems have constant-linear-quadratic propagators of the form:

$$\dot{a}_i = c_i + \sum_{j=1}^N l_{ij} a_j + \sum_{j,k=1}^N q_{ijk} a_j a_k, \quad i = 1, \dots, N. \tag{14}$$

The instantaneous growth of the TKE K is given by

$$\dot{K} = \sum_{i=1}^N a_i \dot{a}_i = \sum_{i=1}^N c_i a_i + \sum_{i,j=1}^N l_{ij} a_i a_j + \sum_{i,j,k=1}^N q_{ijk} a_i a_j a_k. \tag{15}$$

The contribution of the constant term is estimated by the Cauchy-Schwarz inequality

$$\left| \sum_{i=1}^N c_i a_i \right| \leq \|\mathbf{a}\| \|\mathbf{c}\| = \sqrt{2K} \|\mathbf{c}\|, \tag{16}$$

where, $\mathbf{c} = (c_1, \dots, c_N)^T$ and $\|\cdot\|$ denotes the standard Euclidean norm.

Next, the maximum growth due to the linear term is estimated. A decomposition of l_{ij} into a symmetric and antisymmetric part is employed

$$l_{ij} = l_{ij}^S + l_{ij}^A, \quad \text{with } l_{ij}^S \triangleq (l_{ij} + l_{ji})/2, \quad \text{and } l_{ij}^A \triangleq (l_{ij} - l_{ji})/2. \tag{17}$$

The TKE growth due to the linear term is bounded by

$$\left| \sum_{i,j=1}^N l_{ij} a_i a_j \right| = \left| \sum_{i,j=1}^N l_{ij}^S a_i a_j \right| \leq \|\mathbf{a}\|^2 \times \sigma_1(l^S) = 2K \sigma_1(l^S), \tag{18}$$

Table 1 DNS and analysed Galerkin systems

Abbreviation	Description
DNS	Post-transient Navier–Stokes simulation used for the POD model
GS ⁰	Galerkin model (11)
GS ^I	Galerkin model (14) with $N = 20$
GS ^{II}	Same as GS ^I , but with energy-preserving quadratic term $q_{ijk} \triangleq q_{ijk}^A$; see (19) and Sect. 4.2
GS ^{III}	Same as GS ^{II} , but with added nonlinear eddy viscosity (23); see Sect. 4.3

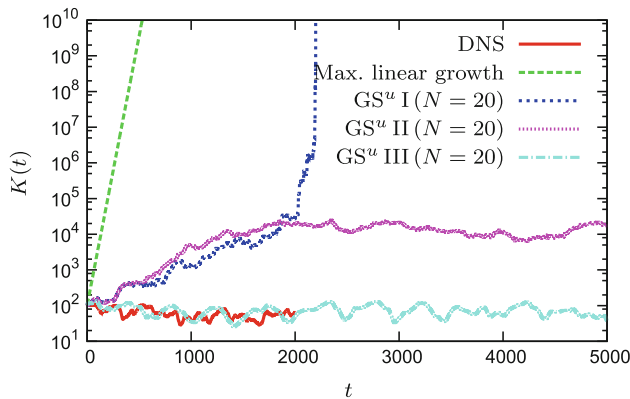


Fig. 3 Evolution of the TKE of the 2D mixing layer. Data of the DNS and of Galerkin systems I–III are displayed (see Table 1 and figure caption)

where $\sigma_1(l^S)$ is the largest real eigenvalue of the matrix $l^S = (l_{ij}^S)_{i,j=1,\dots,N}$.

Finally, the maximum growth due the quadratic term is estimated. We introduce the decomposition of q_{ijk} —in analogy to the linear term—into a symmetric and anti-symmetric part:

$$q_{ijk} = q_{ijk}^S + q_{ijk}^A, \quad \text{with} \quad (19a)$$

$$q_{ijk}^S \triangleq (q_{ijk} + q_{ikj} + q_{jik} + q_{jki} + q_{kij} + q_{kji})/6, \quad \text{and} \quad (19b)$$

$$q_{ijk}^A \triangleq (5q_{ijk} - q_{ikj} - q_{jik} - q_{jki} - q_{kij} - q_{kji})/6. \quad (19c)$$

Moreover, we define the Frobenius norm of a tensor $\mathcal{Q} = (q_{ijk})_{i,j,k=1,\dots,N}$ as

$$\|\mathcal{Q}\|_F \triangleq \sqrt{\sum_{i,j,k=1}^N q_{ijk}^2}. \quad (20)$$

The maximum power of the quadratic term is obtained by repeated application of the Cauchy-Schwarz inequality:

$$\left| \sum_{i,j,k=1}^N q_{ijk} a_i a_j a_k \right| = \left| \sum_{i,j,k=1}^N q_{ijk}^A a_i a_j a_k \right| \leq \|\mathbf{a}\|^3 \|\mathcal{Q}^A\|_F = (2K)^{3/2} \|\mathcal{Q}^A\|_F. \quad (21)$$

Note that estimates (16) and (18) are sharp, in the sense that the equality signs hold for some \mathbf{a} . (21) is also the sharpest estimate for general 3-tensors q_{ijk} .

Summarizing, the maximum growth of the TKE is bounded by

$$\dot{K} \leq \sqrt{2K}\|c\| + 2K\sigma_1(l^S) + (2K)^{3/2}\|\mathcal{Q}^A\|_F. \quad (22)$$

Only the symmetric part of the quadratic term can give rise to a finite-time divergence as numerically observed for Galerkin system I in Fig. 3. This observation is corroborated by the fact that the growth rate of TKE $\sigma^K \triangleq \dot{K}/K$ exceeds $\sigma_1(l^S)$ from the linear term. In Fig. 3, the maximum growth due the linear term is illustrated by $K(t) = K(0)\exp[\sigma_1(l^S)t]$. The slope σ^K is much larger than $\sigma_1(l^S)$ showing the quadratic term at work.

4.2 Symmetries of the Galerkin system

Kraichnan and Chen (1989) investigated the Galerkin system (6) for orthonormal Galerkin expansions (1). They derived that the quadratic term is energy preserving, i.e. $q_{ijk}^S \equiv 0$, for a range of boundary conditions, e.g. steady Dirichlet conditions, ambient flow or free-stream conditions at infinity, or periodic boundary conditions. For the convective boundary condition, this energy-preserving property cannot be rigorously proved. However, the transfer term is numerically observed to vanish consistent with $q_{ijk}^S \equiv 0$. In the following, the quadratic term energy is made energy preserving by replacing q_{ijk} with q_{ijk}^A . The resulting dynamical model is called Galerkin system II (see Table 1). According to (22), a finite-time blow-up is impossible now. Numerically, a bounded solution (see Fig. 3) is observed. However, the energy level is too large since the energy dissipation in higher-order modes is neglected.

We conjecture that the finite-time blow-up of Galerkin system I is caused by a numerical discretization error in q_{ijk} leading to an unphysical q_{ijk}^S component. This conjecture is corroborated by the tendency of decreasing blow-up times with larger values of N . At $N = 50$, for instance, K diverges before $t = 800$. Similar observations have been made for the incompressible turbulent jet (Schlegel et al.

2012). The higher-order modes represent smaller structures and introduce larger discretization errors.

4.3 Nonlinear eddy-viscosity model with guaranteed stability

In the previous section, enforcing an energy-preserving quadratic term has improved the behaviour of the Galerkin system. In the last step, the neglected energy dissipation is accounted for by a single eddy-viscosity model. A constant eddy viscosity, as employed in earlier studies, is unphysical, since it leads to a linear term for a nonlinear energy cascade, i.e. has incorrect scaling characteristics. In fact, the attractor TKE could not be stabilized for long-time intervals with carefully tuned constant eddy viscosities. The FTT closure formalism (Noack et al. 2008) gives rise to a nonlinear eddy-viscosity model (Noack et al. 2011), which has been successfully applied to the turbulent jet (Schlegel et al. 2009) and other flows. This auxiliary model adds a single eddy-viscosity term to the propagator f of (6):

$$\dot{a}_i = f_i(\mathbf{a}) + \nu_T \sqrt{\frac{K(t)}{K_\infty}} l_{ii}^v a_i. \tag{23}$$

Here, the parameter $\nu_T > 0$ is calibrated to yield a TKE K the mean value of which corresponds to the DNS analogue $K_\infty = \sum_{i=1}^N \lambda_i/2$ where λ_i ($i = 1, \dots, N$) are the POD eigenvalues. The square root dependency on K is required by the FTT closure formalism, or even more generally, by scaling arguments (Noack et al. 2011).

The resulting Galerkin system III (see Table 1) is shown to have a guaranteed bounded solution. The new estimate for maximum TKE growth (22) reads

$$\dot{K} \leq \sqrt{2K} \|c\| + 2K\sigma_1(l^S) - \beta K^{3/2}, \tag{24}$$

where β is a positive parameter from the eddy-viscosity term, exploiting $l_{ii}^v < 0$ for $i = 1, \dots, N$. Evidently, the leading term $-\beta K^{3/2}$ is stabilizing. There exist a value K_{\max} such that for $K > K_{\max}$, we have $\dot{K} < 0$. In other words, the attractor of Galerkin system III must be inside the sphere $K \leq K_{\max}$.

Figure 3 shows the TKE evolution of Galerkin solution III. Now, the TKE evolution is qualitatively in good agreement with the DNS data. Moreover, the averaged modal energy levels $\langle K_i(t) \rangle_t = \langle a_i^2(t)/2 \rangle_t$, where $\langle \cdot \rangle_t$ denotes a time average, compare well with the corresponding DNS levels $\lambda_i/2$ (see Fig. 4). Note that a single eddy viscosity is used to characterize a whole energy spectrum. This is a coarse approximation. Further improvements can be obtained from introducing modal eddy viscosities $\nu_{T,i}$ as in Rempfer and Fasel (1994) and

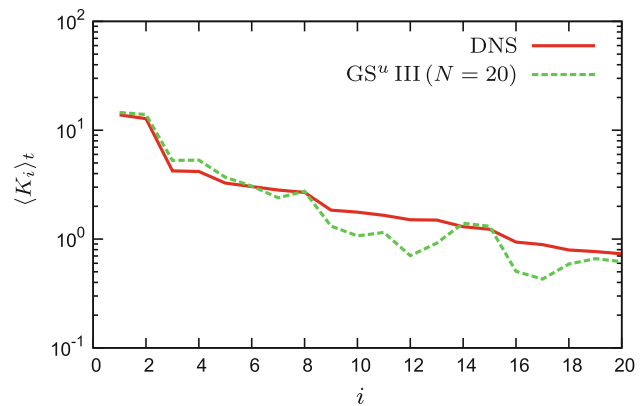


Fig. 4 Energy spectrum for the 2D mixing layer. Data of the DNS and of Galerkin system III are displayed (see Table 1 and figure caption)

Bergmann et al. (2005), or considering eddy-viscosities function of time $\nu_T(t)$ as in Bergmann (2004). This is the subject of the next section.

5 Parameter identification

POD Galerkin models have an accurate short-time behaviour but an imperfect long-time predictability. This is partly due to the truncation errors introduced by neglecting the effect of the high-order modes in the POD expansion. The consequence is an energy accumulation in the model and an amplitude growth of the temporal coefficients. At this point, the quadratic structure of the propagator (Getz and Jacobson 1977) may lead to numerical instabilities of the model producing blow-up in finite time. In this section, it will be demonstrated that this behaviour can be cured by employing data assimilation techniques for identifying whole or part of the parameters which define the model. First, in Sect. 5.1, the main ideas around data assimilation are introduced, followed by the description of the specific approach used in this paper. Then, in Sect. 5.2, data assimilation is first applied to determine all the dynamical system’s coefficients. Finally, in Sect. 5.3, the nonlinear eddy-viscosity model proposed in Sect. 4.3 is considered, and data assimilation is employed to determine optimally the turbulent eddy viscosity ν_T . For that, different numerical strategies are investigated. In Sect. 5.3.1, the artificial eddy viscosity ν_T is first assumed to be dependent only on time. Then, in Sect. 5.3.2, dependency on the POD mode number is added. Finally, in Sect. 5.3.3, the time derivative of the eddy viscosity ν_T is considered as penalization term to make the time evolution of the optimal eddy viscosity more physical.

5.1 Data assimilation

5.1.1 Generalities

Data assimilation is a generic methodology, which combines heterogeneous observations with the underlying dynamical principles governing the system under observation to estimate at best physical quantities. Starting from a background solution and incoming imperfect information, an optimal estimation of the true state of the system is determined, which takes into account the respective statistical confidences of the different observations. By convention, this estimation of the true state is called *analysed* solution. Data assimilation is now routinely used in meteorology to combine images coming from satellites, meteorological observations and a dynamical model in order to forecast the weather (Navon 2009; Titaud et al. 2010). Since numerical weather prediction is an initial value problem, the goal of assimilation is in this case to find the best initial condition of the numerical model that minimizes the observations errors. In fluid mechanics, data assimilation was more recently introduced for estimating quantities (Papadakis 2007) and predicting their time evolutions. There are two basic approaches in data assimilation: stochastic estimation that is based on probability considerations (Kalman filtering for instance), and variational data assimilation, which is used hereafter, where the estimation is found as the solution of an optimization problem. When the observations are distributed in time, this approach is referred as four-dimensional variational assimilation or 4D-Var. In this type of methods, there is an implicit assumption that the model dynamics is perfect (strong constraint, see Sect. 5.1.2), which implies that the only control parameters to improve the fit of the model to the observations are the initial conditions and some model parameters. This assumption may be relaxed by allowing some corrections to the model dynamics. This is achieved by including a forcing term on the right-hand side of the dynamical equations as additional control parameters (see, e.g. Artana et al. 2012). In this formulation, the forcing term is part of the dynamical system meaning that the weak constraint 4D-Var cannot be used to predict the system's dynamics after the end of the assimilation window. For this reason, only strong constraint 4D-Var will be investigated.

The determination of the control parameters relies on a minimization problem where the cost functional is built as a sum of an observation error, which measures the difference between the observations and the output of the identified model, and different background errors, which penalize the variation between the background states and the estimated values. In practice, these different terms can be weighted accordingly on the level of statistical confidence that can be evaluated from expert knowledge. The

solution of this constrained optimization problem is computed through an iterative descent algorithm where the gradient of the cost functional with respect to the variation of the control parameters is found by solving an adjoint problem. Computing the solution of an optimality system is known to be computationally very expensive since the optimal solution is found iteratively by integrating backward in time the adjoint equation (Cordier 2010). However, here, the dynamical model corresponds to a POD ROM and then the computation is numerically tractable (D'Adamo et al. 2007; Artana et al. 2012). In closing, let us remark that the “physical” part of data assimilation is in the definition of the cost functional and of all the ingredients: control parameters, error statistics, norms, observations, etc. Once these ingredients are chosen, the problem is fully determined and the last task for obtaining the analysed solution remains on computational techniques based on gradient-based optimization. This point will be clearly illustrated by the results presented in Sects. 5.2 and 5.3.

5.1.2 Strong constraint 4D-Var

Let X be the state variable and \mathbb{M} be the nonlinear operator relative to the dynamics, the evolution in time of X is given by the following dynamical system:

$$\begin{aligned} \frac{\partial X}{\partial t}(t) + \mathbb{M}(X(t), u) &= 0 \\ X(0) &= X_0^b + \eta, \end{aligned} \quad (25)$$

where X_0^b is an a priori known initial condition of the system, η an initial condition perturbation and u a set of coefficients of the model. Here, the control parameters u are not depending on time but the case of u function of time is a straightforward extension.

Strong constraint assimilation consists of finding the solution $X(t)$ of the dynamical system (25) that is closest at the same time to the observations \mathcal{Y} , obtained at discrete sample times (see Fig. 5), and to regularization terms called *background* terms. The goal is then to find the control parameters (η, u) which minimize the cost functional \mathcal{J} defined as:

$$\begin{aligned} \mathcal{J}(u, \eta) &= \frac{1}{2} \int_0^T \|\mathcal{Y}(t) - \mathbb{H}(X(t; \eta, u))\|_{\mathcal{R}^{-1}}^2 dt \\ &+ \frac{1}{2} \|\eta\|_{\mathcal{B}^{-1}}^2 + \frac{1}{2} \|u - u^b\|_{\mathcal{C}^{-1}}^2, \end{aligned} \quad (26)$$

where T is the optimization window. The nonlinear operator \mathbb{H} , called observation operator, goes from the state space to the observation space. \mathcal{R} , \mathcal{B} and \mathcal{C} are covariance tensors of the observation space, state space and control space. They are related respectively to the observations, the state variables' initial conditions and to the control variables. The norms $\|\cdot\|_{\mathcal{R}^{-1}}$, $\|\cdot\|_{\mathcal{B}^{-1}}$ and $\|\cdot\|_{\mathcal{C}^{-1}}$ are induced norms of the

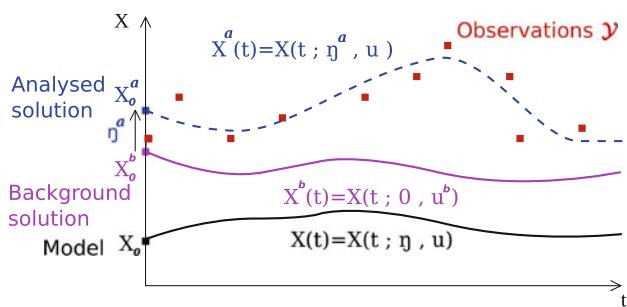


Fig. 5 Schematic representation of 4D-Var

inner products $\langle \mathcal{R}, \cdot \rangle$, $\langle \mathcal{B}, \cdot \rangle$ and $\langle \mathcal{C}, \cdot \rangle$. The role of these covariance tensors is to give more or less confidence in the observations and background states. These tensors have a key influence for combining inhomogeneous sources of information in data assimilation. The covariance tensors may be chosen based on extra knowledge of the system. Here, they have been simply defined as diagonal tensor. The optimal control parameters (η^a, u^a) are called *analysed solutions* and the associated analysed dynamics $X^a(t)$ is the best estimation of the system’s state, solution of (25) according to the criterion (26). The couple $(0, u^b)$ corresponds to the *background solution* of the problem. A schematic description of data assimilation is given in Fig. 5.

The minimization of \mathcal{J} is done using the limited storage variant of the BFGS quasi-Newton algorithm (Gilbert and Lemaréchal 2009). For determining the descent directions, the gradients of the functional with respect to the two control variables η and u need first to be evaluated. The use of finite differences to determine the gradient of the cost functional is in practice unfeasible when the dimension of the state variables is too large. An elegant solution is to write an *adjoint formulation* of the problem. We will see soon that the determination of the gradient of \mathcal{J} with respect to the control variables then corresponds to the forward integration of the dynamical system (25) followed by a backward integration of an adjoint dynamical model to be determined.

In variational data assimilation, the analysed dynamics is found as solution of the constrained minimization problem given by (26) and (25). A classical way for solving this type of constrained optimization problem (Gunzburger 1997) is by introducing a Lagrangian functional \mathcal{L} defined by

$$\mathcal{L}(X(t), u, \eta, \theta(t), \mu) = \mathcal{J}(u, \eta) - \int_0^T \left\langle \frac{\partial X(t)}{\partial t} + \mathbb{M}(X(t), u), \theta(t) \right\rangle dt - \langle X(0) - X_0^b - \eta, \mu \rangle \tag{27}$$

where $\theta(t)$ and μ are two Lagrange multipliers introduced to enforce the constraints given by (25). When the minimum of \mathcal{J} is reached, $\nabla \mathcal{J} = \nabla \mathcal{L} = 0$.

Setting the first variation of \mathcal{L} with respect to X to 0 leads to the adjoint equation

$$-\frac{\partial \theta}{\partial t}(t) + \left(\frac{\partial \mathbb{M}}{\partial X} \right)^* \theta(t) = \left(\frac{\partial \mathbb{H}}{\partial X} \right)^* \mathcal{R}^{-1}(\mathbb{H}(X(t)) - \mathcal{Y}(t)), \tag{28}$$

where $\frac{\partial \mathbb{M}}{\partial X}$ and $\frac{\partial \mathbb{H}}{\partial X}$ denote respectively the linear tangent operator¹ of \mathbb{M} and \mathbb{H} , and $\left(\frac{\partial \mathbb{M}}{\partial X} \right)^*$ and $\left(\frac{\partial \mathbb{H}}{\partial X} \right)^*$ their adjoint operators². The adjoint Eq. (28) is defined backward in time with the terminal condition $\theta(T) = 0$.

Setting the first variation of \mathcal{L} with respect to the control parameters u and η to 0 leads to the optimality conditions

$$\begin{aligned} \frac{\partial \mathcal{J}}{\partial u} &= - \int_0^T \left(\frac{\partial \mathbb{M}}{\partial u} \right)^* \theta(t) dt + \mathcal{C}^{-1}(u - u^b) \quad \text{and} \\ \frac{\partial \mathcal{J}}{\partial \eta} &= \theta(0) + \mathcal{B}^{-1}\eta \end{aligned} \tag{29}$$

The system of coupled differential Eqs. (25), (28) and (29) is called optimality system. This system is in general solved iteratively starting from an initial condition for the control variable (see, e.g. Cordier 2010). Indeed, the optimality conditions can be evaluated to determine the gradient of \mathcal{J} as soon as the Lagrange multipliers are known, it means as soon as the adjoint Eq. (28) is integrated backward in time. However, since (28) is depending on the state variable X , the dynamical system (25) must be first integrated forward in time for a given value of the control parameter.

5.2 Identification of Galerkin system coefficients

Obviously, the dynamical system (14) and its finite-time blow-up fall into the data assimilation framework as presented in Sect. 5.1.1. The temporal coefficients $a_i(t)$ can be considered as state variables $X(t)$. The POD ROM (14) can serve as dynamical model \mathbb{M} and the POD coefficients $a_i^P(t)$ as observations $\mathcal{Y}(t)$. Finally, the coefficients c_i , l_{ij} and q_{ijk} of (14) can be used as control parameters u in the strong constraint 4D-Var. Concerning the background solutions X_0^b and u^b , they can be determined from the temporal coefficients obtained directly by POD ($a_i^P(t = 0)$), and from values determined by Galerkin projection or identification (Cordier et al. 2010), respectively. The strong constraint 4D-Var formulation described in Sect. 5.1.2 can then be easily applied.

¹ The linear tangent of an operator A is the directional derivative operator or Gâteaux derivative of A defined as:

$$\frac{\partial A}{\partial X}(X)\delta X = \lim_{h \rightarrow 0} \frac{A(X + h\delta X) - A(X)}{h} \quad \forall \delta X.$$

² The adjoint A^* of a linear operator A on a space \mathcal{D} is such that $\forall x, y \in \mathcal{D}, \langle Ax, y \rangle = \langle x, A^*y \rangle$.

In that case, the corresponding cost functional reads

$$\mathcal{J}_1(c_i, l_{ij}, q_{ijk}) = \mathcal{M} + \alpha \mathcal{M}_c \quad \text{with} \quad (30a)$$

$$\mathcal{M} = \frac{1}{2} \int_0^T \|\mathbf{a}(t) - \mathbf{a}^P(t)\|^2 dt \quad \text{and} \quad (30b)$$

$$\mathcal{M}_c = \frac{1}{2} (\|\mathbf{c} - \mathbf{c}^0\|^2 + \|\mathbf{L} - \mathbf{L}^0\|_F^2 + \|\mathbf{Q} - \mathbf{Q}^0\|_F^2). \quad (30c)$$

In (30), \mathcal{M} is a measure of the performance criterion to be minimized, and \mathcal{M}_c is a measure of the background errors. The *background* coefficients $c_i^0, l_{ij}^0, q_{ijk}^0$ of (30c) are the values found directly by Galerkin projection. The Frobenius norm is here considered for the matrix \mathbf{L} of the linear coefficients and the tensor \mathbf{Q} of the quadratic coefficients. In (30), the initial conditions of the dynamical system are supposed to be known perfectly. The strong constraint 4D-Var is applied for $N = 20$ as in Sect. 4. The corresponding adjoint equation and optimality conditions are given in Table 2. Since the determination of the gradient of \mathcal{J}_1 by the adjoint formulation requires at least one forward time integration of the model, an iterative procedure is used for minimizing \mathcal{J}_1 where the optimization window is progressively increased from 100 to 2,000 by step of length 10.

The role of the regularization parameter α in (30a) is to balance two requirements: (i) the analysed solutions, here the coefficients of the model, should give a small value of \mathcal{M} , and (ii) the background error \mathcal{M}_c should be small. The computation of the penalization coefficients α which will be used in this section and in Sect. 5.3 is built on the traditional L-curve method (see Hansen 1998, for more details). The L-curve method is based on the analysis of the curve representing \mathcal{M} versus \mathcal{M}_c . In all the cases encountered in this work, this curve exhibits a typical L shape. The corner of the L curve represents a fair compromise between the minimization of \mathcal{M} and of \mathcal{M}_c . In Cordier et al. (2010), the detection was based on the maximization of the curvature of the L-curve as implemented in the package REGULARIZATION TOOLS (Hansen 1994). Here, the detection was made iteratively by testing different values of the penalization parameter α .

The influence of the penalization parameter on the description of the mixing layer TKE is displayed in Fig. 6. For $\alpha = 1$, the analysed solution does not follow the original TKE evolution after approximately half the assimilation window. When α is increased to 10^8 , the model is now sufficiently accurate to reproduce qualitatively well the mixing layer TKE in the assimilation window. However, outside the time window of the database (forecast window), a strong divergence from reference trajectory occurs.

5.3 Identification of a turbulent eddy viscosity

The determination by 4D-Var of all the coefficients of the dynamical system leads to an accurate representation of the TKE over the assimilation window but does not ensure stability of the model on the forecast window (see Sect. 5.2). One way of trying to improve the results of the optimization procedure is to increase the physical reliability of the model. For that, the nonlinear eddy-viscosity model given by (23) can be used. In Sect. 4.3, the parameter v_T was calibrated to yield a mean TKE which corresponds to K_∞ , the value coming from the DNS. In this section, different 4D-Var strategies will be used to determine according to the case an eddy viscosity dependent on time (Sect. 5.3.1, 5.3.3) or function of time and on the POD index number (Sect. 5.3.2).

5.3.1 4D-Var identification of $v_T(t)$

The dynamical system is now considered with the nonlinear turbulent eddy viscosity written in (23), i.e.

$$\begin{aligned} \frac{da_i}{dt} &= c_i + \sum_{j=1}^N l_{ij} a_j + \sum_{j,k=1}^N q_{ijk} a_j a_k + v_T(t) \sqrt{\frac{K(t)}{K_\infty}} l_{ii}^v a_i \\ a_i(0) &= a_i^P(0) + \eta_i. \end{aligned} \quad (31)$$

The objective of the 4D-Var is to find the time-dependent eddy viscosity $v_T(t)$ and the initial condition perturbation $\boldsymbol{\eta}$ that minimize the cost functional given by

$$\begin{aligned} \mathcal{J}_2(\boldsymbol{\eta}, v_T(t)) &= \frac{1}{2} \int_0^T \|\mathbf{a}(t) - \mathbf{a}^P(t)\|^2 dt + \frac{\alpha}{2} \|\boldsymbol{\eta}\|^2 \\ &\quad + \frac{\beta}{2} \int_0^T v_T^2(t) dt. \end{aligned} \quad (32)$$

The strong constraint formalism as described in Sect. 5.1.2 is developed with (31) as dynamical model \mathbb{M} and (32) as cost functional. The adjoint equation and the optimality conditions are given in Table 2. The control parameters are initialized to zero at the beginning of the optimization. The corresponding optimality system is solved with $N = 20$ and $\alpha \triangleq \beta = 10^4$ where α was found with the L-curve method. For these values of the penalization parameters, the POD coefficients and the TKE of the mixing layer database are well reproduced (see Fig. 7). As might be expected at convergence of the 4D-Var, the time evolution of the analysed TKE is weakly depending on the values of the penalization parameters. However, the values of α and β influence strongly the variations of the optimal control parameters. The eddy viscosity shown in Fig. 8(a) appears fairly spiky and irregular. The tendency of the 4D-Var

Table 2 Summary of the optimality systems derived by 4D-Var

Cost functional	State equation	Adjoint equation	Optimality condition
$\mathcal{J}_1(c_i, l_{ij}, q_{ijk}) = \frac{1}{2} \int_0^T \ \mathbf{a}(t) - \mathbf{a}^P(t)\ ^2 dt + \frac{\alpha}{2} (\ \mathbf{c} - \mathbf{c}^0\ ^2 + \ \mathbf{L} - \mathbf{L}^0\ _{\mathbb{F}}^2 + \ \mathbf{Q} - \mathbf{Q}^0\ _{\mathbb{F}}^2)$	$\frac{da_i}{dt} = c_i + \sum_{j=1}^N l_{ij} a_j + \sum_{j,k=1}^N q_{ijk} a_j a_k$ $a_i(0) = a_i^P(0)$	$-\frac{d\theta_i}{dt} = \sum_{k=1}^N \left(\frac{\partial \mathcal{M}}{\partial a} \right)_{ik}^* \theta_k + a_i - a_i^P$ $+ \nu_T(t) l_{ij}^{\nu_i} + \sum_{j=1}^N (q_{ijk} + q_{ikj}) a_j(t)$ <p>with $\left(\frac{\partial \mathcal{M}}{\partial a} \right)_{ik} (t) = l_{ik} + \sum_{j=1}^N (q_{ijk} + q_{ikj}) a_j(t)$</p>	$\frac{\partial \mathcal{L}}{\partial c_i} = \alpha(c_i - c_i^0) + \int_0^T \theta_i(t) dt$ $\frac{\partial \mathcal{L}}{\partial l_{ij}} = \alpha(l_{ij} - l_{ij}^0) + \int_0^T \theta_i(t) a_j(t) dt$ $\frac{\partial \mathcal{L}}{\partial q_{ijk}} = \alpha(q_{ijk} - q_{ijk}^0) + \int_0^T \theta_i(t) a_j(t) a_k(t) dt$
$\mathcal{J}_2(\eta, \nu_T(t)) = \frac{1}{2} \int_0^T \ \mathbf{a}(t) - \mathbf{a}^P(t)\ ^2 dt + \frac{\alpha}{2} \ \eta\ ^2 + \frac{\beta}{2} \int_0^T \nu_T^2(t) dt$	$\frac{da_i}{dt} = c_i + \sum_{j=1}^N l_{ij} a_j + \sum_{j,k=1}^N q_{ijk} a_j a_k + \nu_T(t) \sqrt{\frac{K(t)}{K_\infty}} l_{ii}^{\nu_i} a_i$ $a_i(0) = a_i^P(0) + \eta_i$	$-\frac{d\theta_i}{dt} = \sum_{k=1}^N \left(\frac{\partial \mathcal{M}}{\partial a} \right)_{ik}^* \theta_k + a_i - a_i^P + \nu_T(t) l_{ii}^{\nu_i} \left(\sqrt{\frac{K(t)}{K_\infty}} + \frac{a_i^2}{2\sqrt{K(t)K_\infty}} \right)$	$\frac{\partial \mathcal{L}}{\partial \eta_i} = \alpha \eta_i + \theta_i(0)$ $\frac{\partial \mathcal{L}}{\partial \nu_T(t)} = \beta \nu_T(t) + \sum_{i=1}^N l_{ii}^{\nu_i} \sqrt{\frac{K(t)}{K_\infty}} a_i(t) \theta_i(t)$
$\mathcal{J}_3(\eta, \nu_{T,i}(t)) = \frac{1}{2} \int_0^T \ \mathbf{a}(t) - \mathbf{a}^P(t)\ ^2 dt + \frac{\alpha}{2} \ \eta\ ^2 + \frac{\beta}{2} \sum_{i=1}^N \int_0^T \nu_{T,i}^2(t) dt$	$\frac{da_i}{dt} = c_i + \sum_{j=1}^N l_{ij} a_j + \sum_{j,k=1}^N q_{ijk} a_j a_k + \nu_{T,i}(t) \sqrt{\frac{K(t)}{K_\infty}} l_{ii}^{\nu_i} a_i$ $a_i(0) = a_i^P(0) + \eta_i$	$-\frac{d\theta_i}{dt} = \sum_{k=1}^N \left(\frac{\partial \mathcal{M}}{\partial a} \right)_{ik}^* \theta_k + a_i - a_i^P + \nu_{T,i}(t) l_{ii}^{\nu_i} \left(\sqrt{\frac{K(t)}{K_\infty}} + \frac{a_i^2}{2\sqrt{K(t)K_\infty}} \right)$	$\frac{\partial \mathcal{L}}{\partial \eta_i} = \alpha \eta_i + \theta_i(0)$ $\frac{\partial \mathcal{L}}{\partial \nu_{T,i}(t)} = \beta \nu_{T,i}(t) + l_{ii}^{\nu_i} \sqrt{\frac{K(t)}{K_\infty}} a_i(t) \theta_i(t)$
$\mathcal{J}_4(\eta, \nu_T(t)) = \frac{1}{2} \int_0^T \ \mathbf{a}(t) - \mathbf{a}^P(t)\ ^2 dt + \frac{\alpha}{2} \ \eta\ ^2 + \frac{\beta}{2} \int_0^T \nu_T^2(t) dt$	$\frac{da_i}{dt} = c_i + \sum_{j=1}^N l_{ij} a_j + \sum_{j,k=1}^N q_{ijk} a_j a_k + \nu_T(t) \sqrt{\frac{K(t)}{K_\infty}} l_{ii}^{\nu_i} a_i$ $a_i(0) = a_i^P(0) + \eta_i$	$-\frac{d\theta_i}{dt} = \sum_{k=1}^N \left(\frac{\partial \mathcal{M}}{\partial a} \right)_{ik}^* \theta_k + a_i - a_i^P + \nu_T(t) l_{ii}^{\nu_i} \left(\sqrt{\frac{K(t)}{K_\infty}} + \frac{a_i^2}{2\sqrt{K(t)K_\infty}} \right)$	$\frac{\partial \mathcal{L}}{\partial \eta_i} = \alpha \eta_i + \theta_i(0)$ $\frac{\partial \mathcal{L}}{\partial \nu_T(t)} = -\beta \nu_T(t) + \sum_{i=1}^N l_{ii}^{\nu_i} \sqrt{\frac{K(t)}{K_\infty}} a_i(t) \theta_i(t)$

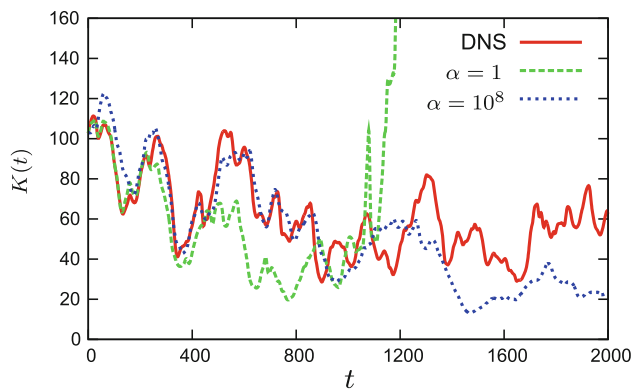


Fig. 6 Evolution of the TKE of the 2D mixing layer. Data of the DNS and of Galerkin systems I with 4D-Var identified coefficients are displayed. Two values of penalization parameter α are compared (see caption)

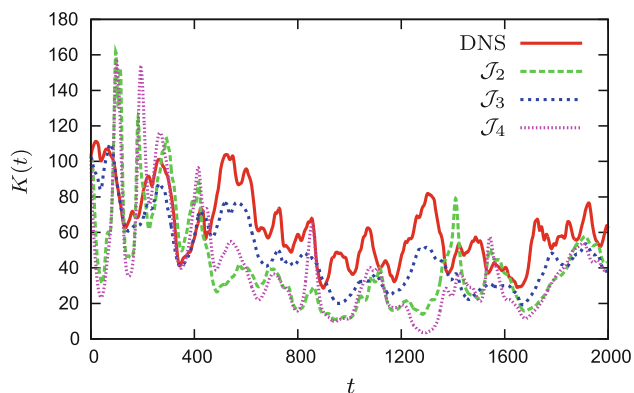


Fig. 7 Evolution of the TKE of the 2D mixing layer. Data of the DNS and of Galerkin systems III with 4D-Var identified turbulent eddy-viscosity terms. Different 4D-Var strategies are compared for determining v_T : (i) minimization of \mathcal{J}_2 , i.e. determination of $v_T(t)$ with a penalization term based on the norm of v_T ($\alpha \triangleq \beta = 10^4$), (ii) minimization of \mathcal{J}_3 , i.e. determination of $v_{T,i}(t)$ with a penalization term based on the norm of v_T ($\alpha \triangleq \beta = 10^4$), (iii) minimization of \mathcal{J}_4 , i.e. determination of $v_T(t)$ with a penalization term based on the norm of the time derivative of v_T ($\alpha \triangleq \beta = 10^6$)

approach to develop spiky controls was also evidenced in other studies (Protas and Styczek 2002; Bergmann et al. 2005). Although the dynamics of the TKE is correctly represented with the optimal eddy viscosity determined by 4D-Var, the fluctuations of v_T are too strong to be considered as physical. Other optimization strategies thus should be considered. First, in Sect. 5.3.2, the eddy viscosity will be made function of the POD index number. Then, in Sect. 5.3.3, the time derivative of the eddy viscosity will be penalized.

5.3.2 4D-Var identification of $v_{T,i}(t)$

The eddy viscosity v_T appearing in (23) is here assumed as depending on time and on the POD index number. This

idea was originally proposed by Rempfer and Fasel (1994) and used in another context in Bergmann (2004) for controlling a cylinder wake flow.

The dynamical system associated with the 4D-Var formalism reads as:

$$\frac{da_i}{dt} = c_i + \sum_{j=1}^N l_{ij}a_j + \sum_{j,k=1}^N q_{ijk}a_ja_k + v_{T,i}(t)\sqrt{\frac{K(t)}{K_\infty}}l_{ii}^v a_i$$

$$a_i(0) = a_i^P(0) + \eta_i, \tag{33}$$

and the cost functional to minimize is

$$\mathcal{J}_3(\boldsymbol{\eta}, v_{T,i}(t)) = \frac{1}{2} \int_0^T \|\mathbf{a}(t) - \mathbf{a}^P(t)\|^2 dt + \frac{\alpha}{2} \|\boldsymbol{\eta}\|^2$$

$$+ \frac{\beta}{2} \sum_{i=1}^N \int_0^T v_{T,i}^2(t) dt. \tag{34}$$

The optimality system given in Table 2 is now solved for $N = 20$ and $\alpha \triangleq \beta = 10^4$. By comparison with the results of Sect. 5.3.1, the dynamics of the POD coefficients for the optimal eddy viscosity is in better agreement with those found directly by the POD analysis of the mixing layer (see “Appendix”). The same behaviour is found for the time evolution of the TKE (see Fig. 7). This increase in accuracy of the analysed model is, however, compensated by an increase in a factor N of the computational cost necessary to solve the 4D-Var problem. Moreover, although the amplitude of the control is reduced compared to Sect. 5.3.1, the variation of the eddy viscosities still remains sufficiently irregular.

5.3.3 4D-Var identification of $v_T(t)$ with penalization of the time derivative

Here, we revisit the case of Sect. 5.3.1 where the eddy viscosity v_T was assumed to be only function of time and penalize in the 4D-Var problem, not the norm of v_T but the norm of its time derivative. The objective is to improve the smoothness of the optimal eddy viscosity by damping high-frequency oscillations of v_T . The cost functional is hence defined as:

$$\mathcal{J}_4(\boldsymbol{\eta}, v_T(t)) = \frac{1}{2} \int_0^T \|\mathbf{a}(t) - \mathbf{a}^P(t)\|^2 dt + \frac{\alpha}{2} \|\boldsymbol{\eta}\|^2$$

$$+ \frac{\beta}{2} \int_0^T \dot{v}_T^2(t) dt. \tag{35}$$

Compared to the optimality system derived in Sect. 5.3.1, only the optimality condition for v_T is modified. This optimality condition now reads

Fig. 8 Time history of the optimal eddy viscosities ν_T determined by minimizing \mathcal{J}_2 with $\alpha \triangleq \beta = 10^4$ (a) and minimizing \mathcal{J}_4 with $\alpha \triangleq \beta = 10^6$ (b)

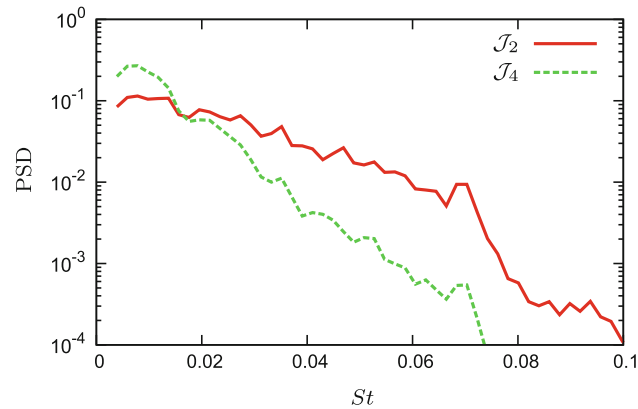
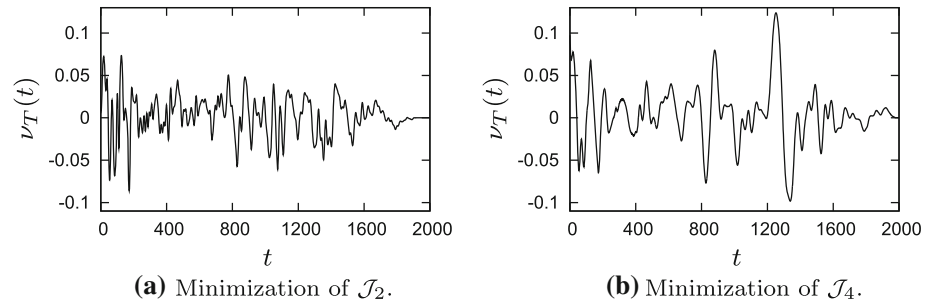


Fig. 9 Power spectral density (PSD) of the optimal eddy viscosities ν_T determined by minimizing \mathcal{J}_2 with $\alpha \triangleq \beta = 10^4$ and minimizing \mathcal{J}_4 with $\alpha \triangleq \beta = 10^6$, see Fig. 8 for their time evolutions. The Strouhal number St is based on the velocity difference across the mixing layer ΔU and on the initial vorticity thickness δ_ω

$$\frac{\partial \mathcal{L}}{\partial \nu_T(t)} = -\beta \ddot{\nu}_T(t) + \sum_{i=1}^N l_{ii}^v \sqrt{\frac{K(t)}{K_\infty}} a_i(t) \theta_i(t). \quad (36)$$

The associated optimality system reported in Table 2 is solved for $N = 20$ with $\alpha \triangleq \beta = 10^6$. The results, in terms of time evolutions of the POD coefficients and TKE (see Fig. 7), are similar to those previously found in Sect. 5.3.1 when the norm of ν_T was penalized. However, the variation of the optimal eddy viscosity is now smoother and the oscillations of ν_T have the same time scale than the first POD modes (see Fig. 8). In Fig. 9, the spectra of the optimal eddy viscosities found by minimizing \mathcal{J}_2 and \mathcal{J}_4 are represented. It is clearly visible that the minimization of \mathcal{J}_4 leads to an attenuation of the higher frequencies, thus reflecting a more physical behaviour of the optimal solution.

To finish, we compared the value of ν_T obtained in Sect. 4.3 by calibration with the mean values resulting from minimizations of \mathcal{J}_2 and \mathcal{J}_4 . These values are perfectly comparable: ν_T was found equal to 8.7×10^{-3} in Sect. 4.3, whereas the mean values of ν_T are equal to 2.2×10^{-3} for the minimization of \mathcal{J}_2 and 3.6×10^{-3} for that of \mathcal{J}_4 .

6 Quantification of statistical bias in POD ROMs

In this section, POD reduced-order models are formulated in a probabilistic framework in order to account for some possible statistical bias leading to an uncertainty of the model coefficients.

6.1 Motivation

In deterministic modelling, a full knowledge of the system (dynamical models, parameters, boundary and initial conditions, geometries, ...) is assumed. For specific choices of inputs, the model then produces unique outputs. However, most physical processes involve some degree of uncertainty. Of course, it is well known that two experiments run under the “same” conditions will yield different results. Uncertainty may also come from incomplete available data (e.g. experimental difficulties) or arise because it is too costly or perhaps impossible to resolve all the scales (e.g. turbulent simulations). In the context of POD ROMs, uncertainty is basically related to the limited samples size used for the POD analysis, which intrinsically bias the knowledge of the full low-dimensional manifold considered. For instance, a too short sampling duration unavoidably disables the prediction of long-term trends, which are needed to ensure a long-term viability of POD ROMs. Some rare key events may also be overrepresented, while other common events are underrepresented or simply locally missing. Since uncertainty is everywhere, it is thus necessary to incorporate a measure of it in the derivation of POD ROMs and possibly use it to correct the dynamical flow during time integration, leading to a reduced-order stochastic model as in Venturi et al. (2008).

In Sect. 6.2, the parametric estimation algorithm proposed in Perret et al. (2006) for identifying the coefficients of the POD ROM is reformulated in a stochastic framework for accounting the sampling error intrinsic to the use of data for identification. For that, a statistical inference procedure known as bootstrap method (Chernick 2008) is first proposed (see Sect. 6.2.1). This method leads by essence to the determination of empirical probability density functions (PDFs) for all the model coefficients (Sect. 6.2.3).

Multivariate PDFs of the values of the coefficients are then introduced in Sect. 6.3.1 and later used in Sect. 6.3.2 to characterize the variability of the short-term solutions obtained by integrating the model for different sets of coefficients. This analysis of uncertainty propagation leads to the definition of a predictable time horizon, relevant for applications in flow control.

6.2 Parametric bootstrap

6.2.1 Description

The principle of parametric bootstrap, as originally introduced by Efron (1979), is illustrated in Fig. 10 for a simple linear regression model $y_i = \beta_1 x_i + \beta_0$ of a set of data points $(x_i, y_i), i = 1, \dots, n$. Using any classical method (e.g. least squares), a first estimation of the unknown parameters β_1 and β_0 can be done by retaining all the points in the data ensemble. This first estimation, classically denoted $\hat{\Theta}^{(0)} = (\hat{\beta}_1^{(0)}, \hat{\beta}_0^{(0)})^T$ where the superscript corresponds to the number of estimation, is statistically biased by the presence of rare events (see Fig. 10a). Our objective is to infer properties of the complete population that yielded the sample $\mathbf{x}^{(0)} = (x_1, \dots, x_n)$ but without knowing the population density function. Statistical inference aims precisely at assessing the accuracy in terms of bias and standard errors of an arbitrary estimate $\hat{\Theta}$ of a parameter Θ of interest knowing only one sample $\mathbf{x}^{(0)}$. The key bootstrap assumption is to consider that the full unknown population is to the sample $\mathbf{x}^{(0)}$ as this sample is to the N_s bootstrap samples $\mathbf{x}^{\star(i)} = (x_1^{\star(i)}, \dots, x_n^{\star(i)})$, $i = 1, \dots, N_s$, obtained from $\mathbf{x}^{(0)}$ by sampling with replacement. For a given bootstrap sample $\mathbf{x}^{\star(i)}$, some values x_j may thus be chosen several times, while others are left out (see Fig. 10b). For each bootstrap sample i , a new estimate $\hat{\Theta}^{\star(i)}$ can be computed. If the number of bootstrap samples is sufficient, then the method converges and provides not only the most probable estimation $\hat{\Theta}$ but also supplies empirical PDFs that can be used to introduce confidence intervals (Fig. 10c).

6.2.2 Application to parameter identification

The parametric bootstrap method, described in Sect. 6.2.1, is here applied to infer the variability of the model coefficients obtained by polynomial identification (Perret et al. 2006). The principle of this method is briefly reviewed. By assumption, the structure of the dynamical model to identify corresponds to a quadratic polynomial as if a standard Galerkin projection of the Navier–Stokes onto the POD modes has been applied (see Sect. 3.1), i.e.

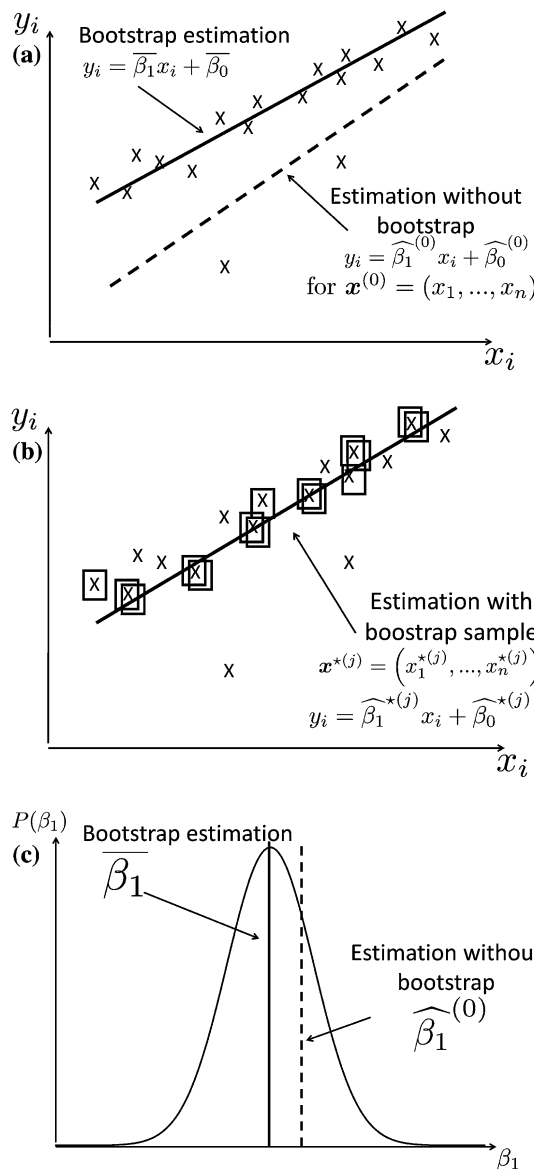


Fig. 10 Principle of parametric bootstrap. Illustration for a linear regression model $y_i = \beta_1 x_i + \beta_0$ fitting a set of data points $(x_i, y_i), i = 1, \dots, n$. **a** Comparison between the bootstrap estimation $(\overline{\beta}_0, \overline{\beta}_1)$ and the estimation $(\hat{\beta}_0^{(0)}, \hat{\beta}_1^{(0)})$ made from $\mathbf{x}^{(0)}$ without any particular precautions; **b** estimation $(\hat{\beta}_0^{\star(j)}, \hat{\beta}_1^{\star(j)})$ made with the bootstrap sample $\mathbf{x}^{\star(j)} = (x_1^{\star(j)}, \dots, x_n^{\star(j)})$; **c** probability density function obtained by bootstrap for the coefficient β_1

$$\dot{a}_i(t) = c_i + \sum_{j=1}^N l_{ij} a_j(t) + \sum_{j,k=1}^N q_{ijk} a_j(t) a_k(t),$$

$$i = 1, \dots, N. \tag{37}$$

From the knowledge at discrete time instants $t_j, j = 1, \dots, N_t$, of the POD coefficients $a_i, i = 1, \dots, N$, (37) can be solved by a least mean square estimation procedure for determining the coefficients c_i, l_{ij}, q_{ijk} . The

minimization problem leads immediately to a system of linear equations:

$$A\mathbf{y}_i = \mathbf{B}_i \quad \text{with } i = 1, \dots, N, \tag{38}$$

where A , independent of i , is the matrix containing all the instantaneous temporal mode monomials $(1, a_i, a_i a_j)$, and \mathbf{B}_i is the vector of the instantaneous values of the time derivative $\dot{a}_i(t_j)$, $j = 1, \dots, N_t$. The vector \mathbf{y}_i , of size $N_{y_i} = 1 + N + N(N + 1)/2$, corresponds to the coefficients of the model (37), and is defined as:

$$\mathbf{y}_i = (c_i, l_{i1}, \dots, l_{iN}, q_{i11}, \dots, q_{iNN})^T. \tag{39}$$

Assuming $N_t \geq N_{y_i}$, a singular value decomposition (SVD) is applied to solve each overdetermined system (37) and compute \mathbf{y}_i . This technique enables to filter out the contribution of the less significant singular values, which would be likely to contaminate the solution in case of ill conditioning of A .

In the bootstrap framework, the parameter Θ corresponds to all the POD coefficients \mathbf{y}_i , i.e. $\Theta = (\mathbf{y}_1, \dots, \mathbf{y}_N)^T$. The total number of model coefficients is then $N_\Theta = N_{y_i} \times N$. In addition, the values x_i discussed in Sect. 6.2.1 are now the POD coefficients a_i discretized in time. Starting from this sample obtained by POD, bootstrap samples are determined, each of them being used for solving (38). The number of bootstrap samples N_s is set high enough to obtain converged estimates of PDF for the model coefficients. In this section, a million of samples were considered.

6.2.3 Statistical variability of POD ROM coefficients

As expected, the PDFs of the coefficients c_i, l_{ij}, q_{ijk} are found to be jointly normally distributed. Figure 11 illustrates the typical variability of values observed for the coefficients. As it could be anticipated, for some coefficients, significant differences are observed between the estimate without bootstrap $\hat{\Theta}^{(0)}$ and the most probable estimation determined using bootstrap $\bar{\Theta}$. In addition, the model parameters whose average is near zero may sometimes have the same probability to be negative or positive and thus to represent opposite intermodal interactions. This clearly indicates that the type of coupling between certain modes may be ambiguous and strongly depends on the particular subpart of the low-dimensional manifold observed. Accordingly, a set of constant coefficients is likely to enforce wrong trends at some time instants. It is worth noting that the observation of such an ambiguous behaviour also supplies a new possible interpretation of the lack of robustness of POD ROMs beyond approximately mid-term prediction, when they are only based on constant

coefficients. It supports the consideration that additional nonconstant corrective terms are required to compensate for this intrinsic uncertainty.

6.3 Stochastic POD ROMs

6.3.1 Statistical modelling of POD ROM coefficients

The observation of a jointly Gaussian behaviour associated with the statistical variability of the model coefficients leads to a simple mean to represent POD ROMs in a stochastic framework. Accordingly, the range of probable values for each coefficient Θ_i , $i = 1, \dots, N_\Theta$, of Θ can be described by a normal law $\mathcal{N}(\bar{\Theta}_i, \sigma_i^2)$:

$$p(\Theta_i) = \frac{1}{\sigma_i \sqrt{2\pi}} \exp\left(-\frac{(\Theta_i - \bar{\Theta}_i)^2}{2\sigma_i^2}\right),$$

where the standard deviations σ_i of Θ_i are determined as the square root of the diagonal terms of the covariance matrix, given by:

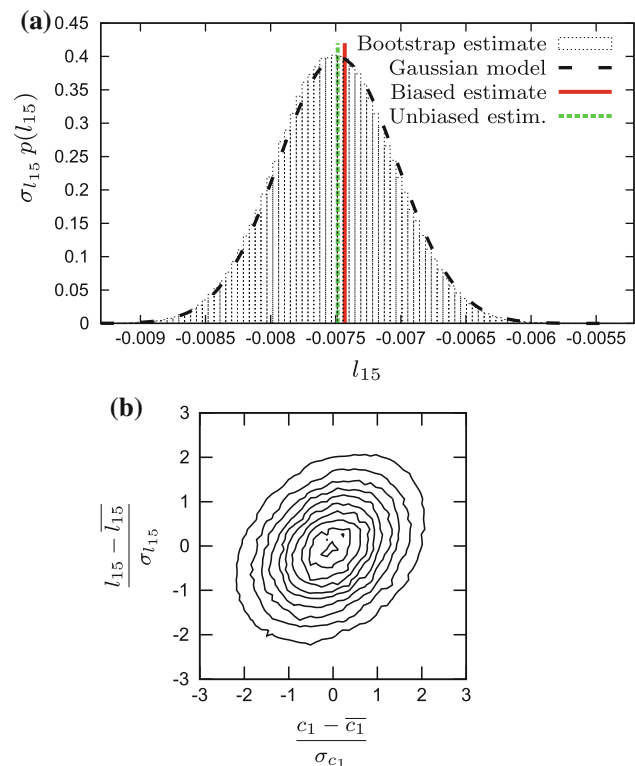


Fig. 11 Stochastic description of the POD ROM coefficients. **a** Comparison for l_{15} between the bootstrap estimation of PDF, the Gaussian model, the biased estimate and the unbiased estimate; **b** normalized joint probability distribution of reduced centred coefficients c_1 and l_{15} (values from 0.01 to 0.16 by increment of 0.01)

$$\Sigma = \left[\Sigma_{ij} \right]_{N_{\Theta} \times N_{\Theta}} = \left[\frac{1}{N_s - 1} \sum_{k=1}^{N_s} \left(\hat{\Theta}_i^{\star(k)} - \bar{\Theta}_i \right) \left(\hat{\Theta}_j^{\star(k)} - \bar{\Theta}_j \right) \right]_{N_{\Theta} \times N_{\Theta}} \tag{40}$$

In order to account for the correlation between coefficients, a multivariate normal law $\mathcal{N}(\bar{\Theta}, \Sigma)$ is introduced:

$$\mathcal{N}(\bar{\Theta}, \Sigma) = \frac{1}{(2\pi)^{N_{\Theta}/2} |\Sigma|^{1/2}} \exp \left(-\frac{1}{2} (\Theta - \bar{\Theta})^T \Sigma^{-1} (\Theta - \bar{\Theta}) \right) \tag{41}$$

where $|\Sigma|$ stands for the determinant of Σ .

6.3.2 Uncertainty propagation

In this section, the uncertainty found by bootstrap analysis in Sect. 6.2.3 for the model coefficients is investigated to determine how it propagates in (37). For this, a family of equiprobable sets of coefficients that follow statistically the multivariate normal law (41) identified in Sect. 6.3.1 has been generated. The propagation of uncertainty is here evaluated for the mixing layer of Sect. 2 based on a POD ROM derived with $N = 10$ ($N_{y_i} = 66$). Contrary to the previous sections, where reduced-order models of dimension 20 have systematically been considered, the polynomial identification technique used in Sect. 6.2.2 is not sufficiently well conditioned to determine reduced-order models of dimension higher than 10. The family of stochastic coefficients has been generated by a two-step procedure. First, a Box–Muller transform (Box and Muller 1958) has been used for determining coefficients following independently normal distributions. Then, a linear change of variables, based on the average coefficients $\bar{\Theta}$ and the Cholesky decomposition of the covariance matrix Σ , has been employed to enforce the correct centring and interdependency relationships of the coefficients (Gentle et al. 2004). This approach which is traditional in the statistics literature could be easily replaced in the future by more sophisticated stochastic techniques.

A fourth-order Runge–Kutta method is then used to integrate in time with the same known initial condition the POD ROMs corresponding to different sets of coefficients. As outputs, a series of equiprobable trajectories in phase space is obtained. A few solutions are illustrated in Fig. 12 for the time evolution of the first POD coefficient a_1 . Most solutions closely follow the expected time evolution of the reference POD coefficient over the short-term horizon. However, for the long-term evolution, the majority of the solutions diverge after a few oscillations, while a few ones outlive during periods larger than the period corresponding

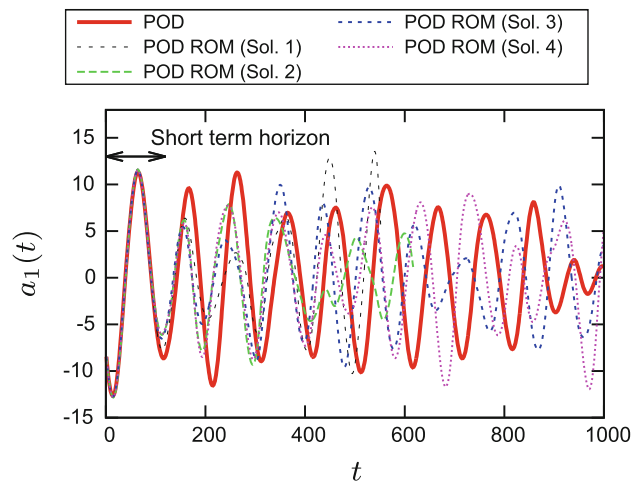


Fig. 12 Uncertainty propagation. Evolutions of a_1 obtained by integration of the POD ROM (37) for different equiprobable sets of coefficients

to the known original signals, eventually reaching artificial limit cycles. An estimation of the decorrelation time of these equiprobable solutions may be given by observing the time evolutions of Fig. 12. This time duration might be considered as the true short-term foreseeable time horizon and used as a reference to determine the period after which any ROM should be updated to keep on representing correctly the flow evolution.

6.4 Perspectives

The bootstrap analysis reveals (see Sect. 6.2.3) that the statistical variability of POD ROM coefficients may lead to ambiguous intermodal relationships. This result legitimates the need to account for the stochastic nature of the coefficients during the time integration of POD ROMs. Such a strategy was recently proposed in Lehnasch and Delville (2011) where a Monte Carlo method was used to foresee simultaneously probable short-term solutions by replicating regularly model coefficients. It was shown in the case of a low Reynolds spatially developing three-dimensional mixing layer flow that it can help both to compensate for the lack of intrinsic stabilization and to sustain correct physical properties. The application of such trial-and-error strategy to more complex flows yet remains unclear since the range of uncertainty appears to increase rapidly with the flow complexity.

7 Summary

Relying on phenomenological approaches (opposition control for instance) to develop a control strategy is limited in practice to a given class of flow configurations or leads

to poor performance. If the goal is to obtain better, faster, cheaper and generally optimal performance over a wide range of operating conditions, model-based control is crucial. In turbulence, reduced-order models based on POD modes are often used to approximate in sufficient details the input-output behaviour of the flow. However, these POD ROMs are known to be relatively fragile when used for control design. Several reasons can be put forward. First, the question of educing physically relevant structures in flow control is extremely difficult since by definition, the flow dynamics will be fully modified by the introduction of the control. Then, the POD modes and their optimality in terms of energy representation are not necessarily the most appropriate. Second, the coefficients of the reduced-order model or the initial conditions of the dynamical system may be not sufficiently well determined to reproduce qualitatively well the dynamics of the controlled flow. Third, when Dirichlet boundary conditions are used for the boundary control, entering explicitly the forcing term in the reduced-order model is not straightforward and special care needs to be taken. In order to evaluate the relative influence of the control modelling and of the POD ROM approach in the difficulties met in the fine description of a flow, we returned to a simple uncontrolled flow that of an incompressible 2D mixing layer.

We have shown that POD ROMs for which the coefficients were calculated explicitly by Galerkin projection do not represent correctly the time evolution of the TKE corresponding to the DNS solution. This is true with a dynamical model derived by Galerkin projection onto the vorticity equation, and this is also true with a Galerkin projection onto the Navier–Stokes equations where it leads for some values of N to finite-time blow-ups. These divergences were analysed in terms of the maximum growth rate of the Galerkin system TKE. It was demonstrated analytically that this behaviour cannot be explained by the linear terms but by the quadratic terms. Following a result of Kraichnan and Chen (1989) who proved that the quadratic nonlinearity is energy preserving, we modified the dynamical system by symmetrizing the quadratic terms. The behaviour of the model was considerably improved in the sense that finite-time blow-ups were no longer observed but the TKE level was still overestimated. Subsequently, we proposed a nonlinear eddy-viscosity model. It was shown that the resulting POD ROM presents a guaranteed bounded solution and a qualitative good agreement with the TKE time evolution determined by DNS. To improve the behaviour of this eddy-viscosity model, we then proposed various 4D-Var optimization strategies. Essentially, the objective was to identify based on different criteria the optimal evolution for the free parameter v_T . For this parameter to be physically relevant, it is necessary that the optimal solution leads at the same time to a good

description of the TKE coming from the DNS and that it is not too rapidly oscillating in time. For that, we proposed in particular a 4D-Var formulation in which the norm of the time derivative of v_T was penalized. This specific approach led in practice (see numerical results in “Appendix”) to the best compromise in terms of temporal descriptions and physical relevance of the eddy viscosity. Finally, we tried to take into account the bias inherent of the sampling employed in the identification techniques. For this purpose, we have used a statistical inference procedure known as bootstrap method. This approach gives us the possibility of determining joined probability density functions for all the coefficients of the model. In a last step, we reformulate the system of quadratic differential equations in a stochastic framework and studied the influence on the long-term solution of different equiprobable sets of coefficients. By averaging all these solutions, a decorrelation time corresponding to the true short-term foreseeable time horizon was defined.

Acknowledgments This work has received support from the National Agency for Research on references ANR-08-BLAN-0115-01 (CORMORED) and ANR-10-CEXC-015-01 (Chair of Excellence TUCOROM). BRN also acknowledges the University of New South Wales at the Australian Defense Force Academy for a Rector-Funded Visiting Fellowship.

Appendix: Comparative remarks of the POD ROMs

A fair selection of the best identification technique for reduced-order models is a difficult task since many, sometimes antagonistic, criteria exist. In Wang et al. (2012), the performances of POD ROMs derived with different closure models are judged on five criteria: the kinetic energy spectrum, the mean velocity components, the Reynolds stresses, the root mean square values of the velocity fluctuations, and the time evolutions of the POD coefficients. In this appendix, due to space limitations, the POD ROMs obtained from Sect. 4.3 to Sect. 6 are quantitatively compared on only two criteria: the time evolutions of the POD coefficients a_1 and a_3 (see Fig. 13), and the power spectra of these POD coefficients (see Fig. 14). The temporal evolutions of the turbulent kinetic energy are moreover used throughout the paper as main criterion of comparison.

From the point of view of temporal behaviour, the worst method is without any doubt the bootstrap technique developed in Sect. 6.2. The 4D-Var identification methods of Sect. 5 behave similarly, a light advantage going to the minimizations of \mathcal{J}_1 and \mathcal{J}_3 at the end of the time window. The identification of a turbulent eddy-viscosity function of time and on the POD index numbers (cost functional \mathcal{J}_3) permits to obtain as good performances as the determination

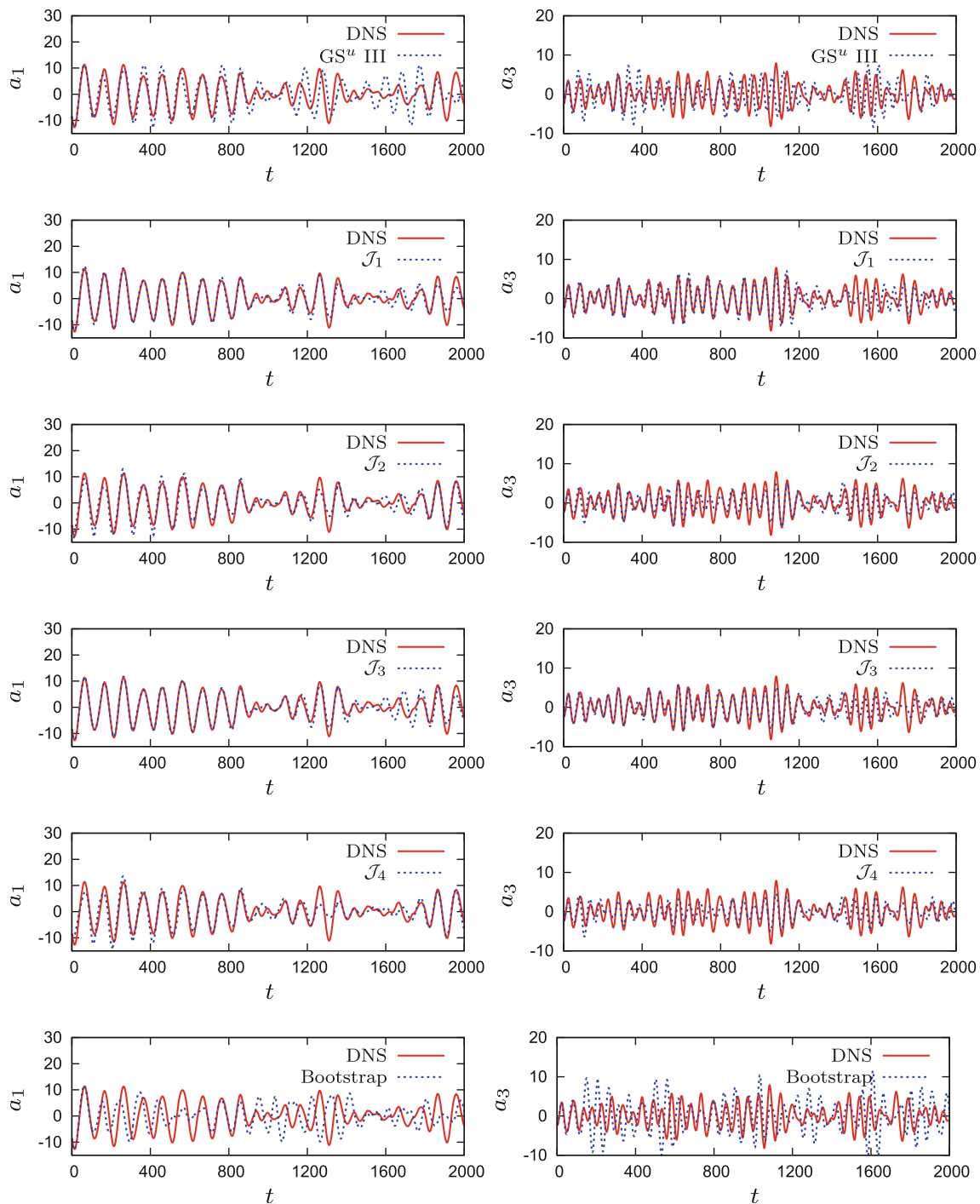


Fig. 13 Time evolutions of the POD coefficients a_1 (left) and a_3 (right) for the different identification approaches considered. $N = 20$ is used for all the methods except for the bootstrap where $N = 10$ was employed. All the results are compared with those obtained by DNS

of all the coefficients of the POD model carried out by minimizing \mathcal{J}_1 . In addition, if the physical behaviour of the analysed turbulent viscosity is the most important, or if the numerical cost for solving the 4D-Var problem is central in the choice of the identification method, then it is preferable to minimize \mathcal{J}_4 rather than \mathcal{J}_3

since the results are equivalent in terms of accuracy. From the point of view of frequential behaviour, it seems that the results are opposite to those obtained for the temporal evolutions. Indeed, it is now the bootstrap technique, which permits to represent the best the spectra obtained directly from the POD coefficients. However, to moderate this

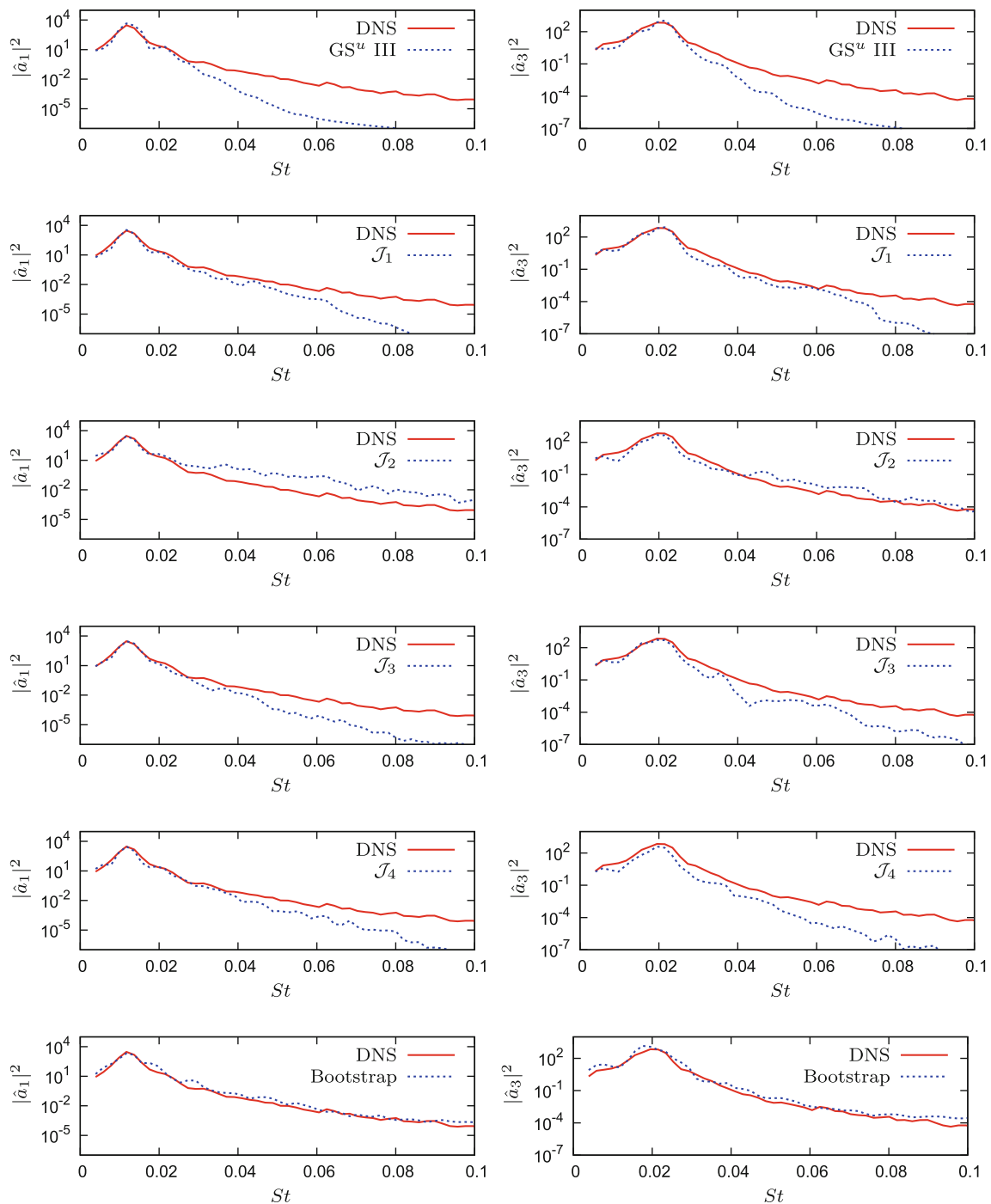


Fig. 14 Power spectra of the POD coefficients a_1 (left) and a_3 (right) for the different identification approaches considered. $N = 20$ is used for all the methods except for the bootstrap where $N = 10$ was employed. All the results are compared with those obtained by DNS

result, it is necessary to remember that for this identification method, the number of modes kept in the POD ROM was only equal to 10 compared to 20 for the other techniques. Likewise, it is now the minimization of the cost functional \mathcal{J}_2 , which leads to the best frequential representation. For the moment, this behaviour is not explained and it would

deserve thorough studies. To conclude this comparison, it is important to note that all the identification techniques based on the determination of eddy-viscosities function of time have no predictive character. A way of curing this limitation consists in taking the time average of the eddy viscosities thus obtained. As for them, the identification techniques

relying on the determination of the model coefficients can be used to predict the dynamics of the system beyond the training window. From this point of view, the advantage is surely to the bootstrap technique since it can result intrinsically in the modification of the model coefficients during numerical integration.

References

- Artana G, Cammilleri A, Carlier J, Mémin E (2012) Strong and weak constraint variational assimilations for reduced order fluid flow modeling. *J Comp Phys* 231:3264–3288
- Aubry N, Holmes P, Lumley JL, Stone E (1988) The dynamics of coherent structures in the wall region of a turbulent boundary layer. *J Fluid Mech* 192:115–173
- Balajewicz M, Dowell EH, Noack BR (2013) Low-dimensional modelling of high Reynolds number shear flows incorporating constraints from the Navier-Stokes equation. Submitted to *J Fluid Mech*
- Bergmann M (2004) Optimisation aérodynamique par réduction de modèle POD et contrôle optimal. Application au sillage laminaire d'un cylindre circulaire. PhD thesis, Institut National Polytechnique de Lorraine, Nancy, France
- Bergmann M, Cordier L, Brancher JP (2005) Optimal rotary control of the cylinder wake using POD Reduced Order Model. *Phys Fluids* 17(9):097,101:1–21
- Bogey C (2000) Calcul direct du bruit aérodynamique et validation de modèles acoustiques hybrides. PhD thesis, Ecole Centrale Lyon
- Box G, Muller M (1958) A note on the generation of random normal deviates. *Ann Math Stat* 29:610–611
- Cavaliere A, Daviller G, Comte P, Jordan P, Tadmor G, Gervais Y (2011) Using large eddy simulation to explore sound-source mechanisms in jets. *J Sound Vib* 330:4098–4113
- Chernick MR (2008) Bootstrap methods: a guide for Practitioners and Researchers, 2nd edn. Wiley, New Jersey
- Colonius T, Lele SK, Moin P (1993) Boundary conditions for direct computation of aerodynamic sound generation. *AIAA J* 31:1574–1582
- Comte P, Silvestrini J, Bégou P (1998) Streamwise vortices in Large-Eddy Simulations of mixing layer. *Eur J Mech B* 17:615–637
- Cordier L (2010) Flow control and constrained optimization problems. In: Noack BR, Morzyński M, Tadmor G (eds) *Reduced-order modelling for flow control*, Springer, Berlin, pp 1–76
- Cordier L, Abou El Majd B, Favier J (2010) Calibration of POD Reduced-Order models using Tikhonov regularization. *Int J Numer Meth Fluids* 63(2)
- D'Adamo J, Papadakis N, Mémin E, Artana G (2007) Variational assimilation of POD low-order dynamical systems. *J Turbul* 8(9):1–22
- Daviller G (2010) Étude numérique des effets de température dans les jets simples et coaxiaux. PhD thesis, École Nationale Supérieure de Mécanique et d'Aérotechnique
- Efron B (1979) Bootstrap methods: another look at the jackknife. *Ann Stat* 7:1–26
- Fletcher CAJ (1984) *Computational Galerkin methods*, 1st edn. Springer, New York
- Galletti G, Bruneau CH, Zannetti L, Iollo A (2004) Low-order modelling of laminar flow regimes past a confined square cylinder. *J Fluid Mech* 503:161–170
- Gatski TB, Bonnet JP (2013) *Compressibility, turbulence and high speed flow*, 2nd edn. Academic Press, Waltham
- Gentle JE, Härdle W, Mori Y (2004) *Handbook of computational statistics: concepts and methods*. Springer, Berlin
- Getz WM, Jacobson DH (1977) Sufficiency conditions for finite escape times in systems of quadratic differential equations. *J Inst Math Applics* 19:377–383
- Gilbert J, Lemaréchal C (2009) *The module M1QN3 – Version 3.3*. INRIA Rocquencourt & Rhône-Alpes
- Gottlieb D, Turkel E (1976) Dissipative two-four method for time dependent problems. *Math Comp* 30(136):703–723
- Gunzburger MD (1997) Introduction into mathematical aspects of flow control and optimization. In: *Lecture series 1997–05 on inverse design and optimization methods*, Von Kármán Institute for Fluid Dynamics
- Hansen PC (1994) Regularization tools: a MATLAB package for analysis and solution of discrete ill-posed problems. *Numer Algorith* 6:1–35
- Hansen PC (1998) Rank-deficient and discrete ill-posed problems: numerical aspects of linear inversion. SIAM, Philadelphia
- Hayder ME, Turkel E (1993) High-order accurate solutions of viscous problem. In: *AIAA paper 93-3074*
- Holmes P, Lumley JL, Berkooz G, Rowley CW (2012) *Turbulence, coherent structures, dynamical systems and symmetry*, 2nd edn. Cambridge University Press, Cambridge
- Joseph DD (1976) *Stability of fluid motions I & II*. Springer Tracts in Natural Philosophy, vol 26 & 27, Springer, Berlin
- Kraichnan RH, Chen S (1989) Is there a statistical mechanics of turbulence? *Phys D* 37:160–172
- Krstic M, Krupadanam A, Jacobson C (1999) Self-tuning control of a nonlinear model of combustion instabilities. *IEEE Tr Contr Syst Technol* 7(4):424–436
- Ladyzhenskaya OA (1963) *The mathematical theory of viscous incompressible flow*, 1st edn. Gordon and Breach, New York
- Lehnasch G, Delville J (2011) A stochastic low-order modelling approach for turbulent shear flows. In: *Seventh symposium on turbulent shear flow phenomena*, Ottawa
- Lodato G, Domingo P, Vervisch L (2008) Three-dimensional boundary conditions for direct and large-eddy simulation of compressible viscous flows. *J Comp Phys* 227(10):5105–5143
- Lugt H (1996) *Introduction to vortex theory*. Vortex Flow Press, Potomac
- Navon I (2009) Data assimilation for numerical weather prediction: a review. *Data Assimilation Atmos Ocean Hydrol Appl* 18(475): 326
- Noack BR, Eckelmann H (1994) A global stability analysis of the steady and periodic cylinder wake. *J Fluid Mech* 270:297–330
- Noack BR, Afanasiev K, Morzyński M, Tadmor G, Thiele F (2003) A hierarchy of low-dimensional models for the transient and post-transient cylinder wake. *J Fluid Mech* 497:335–363
- Noack BR, Papas P, Monkewitz PA (2005) The need for a pressure-term representation in empirical Galerkin models of incompressible shear flows. *J Fluid Mech* 523:339–365
- Noack BR, Schlegel M, Ahlborn B, Mutschke G, Morzyński M, Comte P, Tadmor G (2008) A finite-time thermodynamics of unsteady fluid flows. *J Non Equilib Thermodyn* 33:103–148
- Noack BR, Morzyński M, Tadmor G (eds) (2011) *Reduced-order modelling for flow control*. No. 528 in *CISM Courses and Lectures*, Springer, Berlin
- Papadakis N (2007) *Assimilation de données images : application au suivi de courbes et de champs de vecteurs*. PhD thesis, Université Rennes I
- Perret L, Collin E, Delville J (2006) Polynomial identification of POD based low-order dynamical system. *J Turbul* 7:1–15
- Protas B, Styczek A (2002) Optimal rotary control of the cylinder wake in the laminar regime. *Phys Fluids* 14(7):2073–2087
- Rempfer D (2000) On low-dimensional Galerkin models for fluid flow. *Theoret Comput Fluid Dyn* 14:75–88

- Rempfer D, Fasel FH (1994) Dynamics of three-dimensional coherent structures in a flat-plate boundary-layer. *J Fluid Mech* 275: 257–283
- Rowley CW, Mezić I, Bagheri S, Schlatter P, Henningson D (2009) Spectral analysis of nonlinear flows. *J Fluid Mech* 645: 115–127
- Schlegel M, Noack BR, Comte P, Kolomenskiy D, Schneider K, Farge M, Scouten J, Luchtenburg DM, Tadmor G (2009) Reduced-order modelling of turbulent jets for noise control. In: Numerical simulation of turbulent flows and noise generation: results of the DFG/CNRS Research Groups FOR 507 and FOR 508, Notes on Numerical Fluid Mechanics and Multidisciplinary Design (NNFM), Springer, Berlin, pp 3–27
- Schlegel M, Noack BR, Jordan P, Dillmann A, Gröschel E, Schröder W, Wei M, Freund JB, Lehmann O, Tadmor G (2012) On least-order flow representations for aerodynamics and aeroacoustics. *J Fluid Mech* 697:367–398
- Schmid PJ (2010) Dynamic mode decomposition for numerical and experimental data. *J Fluid Mech* 656:5–28
- Sirisup S, Karniadakis G (2004) A spectral viscosity method for correcting the long-term behavior of POD models. *J Comp Phys* 194:92–116
- Titaut O, Vidard A, Souopgui I, Le Dimet F (2010) Assimilation of image sequences in numerical models. *Tellus A* 62(1):30–47
- Ukeiley L, Cordier L, Manceau R, Delville J, Bonnet JP, Glauser M (2001) Examination of large-scale structures in a turbulent plane mixing layer. Part 2. Dynamical systems model. *J Fluid Mech* 441:61–108
- Venturi D, Wan X, Karniadakis G (2008) Stochastic low dimensional modeling of random laminar wake past a circular cylinder. *J Fluid Mech* 606:339–367
- Wang Z, Akhtar I, Borggaard J, Iliescu T (2012) Proper orthogonal decomposition closure models for turbulent flows: a numerical comparison. *Comput Methods Appl Mech Engrg* 237–240:10–26
- Wei M (2004) Jet noise control by adjoint-based optimization. PhD thesis, University of Illinois at Urbana-Champaign
- Wiener N (1948) *Cybernetics or control and communication in the animal and the machine*, 1st edn. MIT Press, Boston
- Wu JZ, Ma HY, Zhou MD (2006) *Vorticity and vortex dynamics*, 1st edn. Springer, Berlin